Saudi Pharmaceutical Journal 31 (2023) 29–54

HOSTED BY

Contents lists available at ScienceDirect

Saudi Pharmaceutical Journal

journal homepage: www.sciencedirect.com

Original article

Gefitinib-loaded starch nanoparticles for battling lung cancer: Optimization by full factorial design and *in vitro* cytotoxicity evaluation

Haitham Amin [a,*], Shaaban K. Osman [a], Ahmed M. Mohammed [a], Gamal Zayed [a,b]

[a] Department of Pharmaceutics and Pharmaceutical Technology, Faculty of Pharmacy, Al-Azhar University, Assiut 71524, Egypt
[b] Al-Azhar Centre of Nanosciences and Applications (ACNA), Al-Azhar University, Assiut 71524, Egypt

ARTICLE INFO

Article history:
Received 21 July 2022
Accepted 7 November 2022
Available online 15 November 2022

Keywords:
Starch nanoparticles
Lung cancer
Gefitinib
Cellular drug uptake
Flow cytometric assay
Full factorial design

ABSTRACT

Lung cancer is the number one killer among all cancer types. For decades, clinicians have been using conventional chemotherapeutics, but they can't rely on them alone anymore, because they poison bad cells and good cells as well. Researchers exploited nanotechnology as a potential tool to develop a platform for drug delivery to improve therapeutic efficiency. A quality by design synthesis of gefitinib-loaded starch nanoparticles (Gef-StNPs) has emerged as an essential tool to study and optimize the factors included in their synthesis. Therefore, we applied design of experiment (DOE) tools to attain the essential knowledge for the synthesis of high-quality Gef-StNPs that can deliver and concentrate the gefitinib (Gef) at A549 cells, thereby improving therapeutic efficacy and minimizing adverse effects. The *in vitro* cytotoxicity after exposing the A549 human lung cancer cells to the optimized Gef-StNPs was found to be much higher than that of the pure Gef (IC_{50} = 6.037 ± 0.24 and 21.65 ± 0.32 µg/mL, respectively). The optimized Gef-StNPs formula showed superiority over the pure Gef regarding the cellular uptake in A549 human cell line (3.976 ± 0.14 and 1.777 ± 0.1 µg/mL) and apoptotic population (77.14 ± 1.43 and 29.38 ± 1.11 %), respectively. The results elucidate why researchers have a voracious appetite for using natural biopolymers to combat lung cancer and paint an optimistic picture of their potential to be a promising tool in battling lung cancer.

1. Introduction

Cancer has become a major hot spot for research due to its debilitating effect on human health and crippling effect on governments' economies. The U.S. government alone has spent over $100 billion on cancer research since the 1970s with limited progress regarding patients' survival. Cancer is the major cause of death globally after heart diseases. The WHO reported 10 million deaths from cancer in 2020. Among all cancer types, lung cancer is the main cause of cancer death (Bade and dela Cruz, 2020). Lung cancer alone is responsible for 25% of all cancer deaths. Lung cancer annual deaths far outnumber prostate, breast, and colon cancers combined (Sukumar et al., 2013). These data urge researchers to figure out a solution to save patients' lives.

So far, scientists are suffering a defeat in the battle against lung cancer, because they are doing a terrible job of using conventional chemotherapeutics which are vulnerable to degradation by the acidic environment of the stomach, and by enzymes in the bloodstream. Besides, the body barriers hinder cancer drugs from reaching their targets. Therefore, exposing patients to off-target actions "hurt normal cells". The side effects of cancer drugs are crisis on top of crisis for cancer patients because the patient suffers from the adverse effects of cancer drugs besides the cancer itself. Therefore, traditional cancer drugs give us a false sense of security in combating lung cancer, and they are among the worst performers (Anand et al., 2022).

The rapid development of nanomedicine research has offered some grounds for optimism (Martins et al., 2020; Wolfram and Ferrari, 2019). Cancer drugs without nanoparticles are quickly washed out of the body through the kidneys (Peterson et al., 2017), so they don't have time to reach the tumor, but if we place them inside nanoparticles, they won't get washed out by the body, having more time to find the tumor. Therefore, nanoparticles take

* Corresponding author.
E-mail addresses: haithamamin.4522@azhar.edu.eg (H. Amin), shaabanosman@azhar.edu.eg (S.K. Osman), ahmedabdelaal@azhar.edu.eg (A.M. Mohammed), gamalzayed@azhar.edu.eg (G. Zayed).

Peer review under responsibility of King Saud University.

Production and hosting by Elsevier

https://doi.org/10.1016/j.jsps.2022.11.004

center stage in the therapy of lung cancer. Moreover, they could minimize the adverse effects of traditional cytotoxic drugs and could help cancer patients tremendously. However, a major challenge of many nanoparticle types being labeled by the body as foreign. Therefore, they got stuck inside the liver and destroyed. Natural nanoparticles are less likely to be engulfed by immune cells in the liver, they are capable to escape the liver barrier (Anand et al., 2022; C. H. Lin et al., 2017). They don't get recognized by the liver and end up inside the heart of the tumor.

Gef is an orally administered drug that inhibits the tyrosine kinase domain of the epidermal growth factor receptor(Jeannot et al., 2018). Gef is a first-line therapy against locally advanced or metastatic non-small cell lung cancer that has been granted FDA approval in 2015(Q. Lin et al., 2017). However, the downsides of oral Gef are tremendous. First and foremost, it can't effectively target tumor tissue due to slow intestinal absorption, poor water solubility, and poor bioavailability which will compromise the therapeutic efficacy (Garizo et al., 2021). Second, Gef has a large volume of distribution which will extend its adverse effects: hepatotoxicity, interstitial lung disease, and skin toxicity (Galimont-Collen et al., 2007), and finally, lead to therapy withdrawal. Therefore, it is crucial to develop an effective and safer formulation of Gef.

Biopolymers-based nanoparticles could infuse researchers, and hence patients with optimism regarding their safety, biocompatibility, biodegradability, and efficacy.

Starch is the most abundant biopolymer in nature second to cellulose. Soluble starch is utilized to prepare StNPs to convert poorly soluble, poorly absorbed, highly toxic Gef into more water-soluble, more absorbed, and safer and more effective anticancer drug (Wang et al., 2020; Xia et al., 2020; Aghda, n.d.; Wang et al., 2020; Xia et al., 2020). Contrary to Gef therapy alone, nanoparticles could identify the bad cells and save the healthy ones. Thanks to the enhanced permeation and retention effects (EPR), the so-called passive targeting, which relies on the existence of fenestrations in the tumor blood vessels (in the endothelium). These fenestrations permit the passage of the nanoparticles into the cancer cells (enhanced permeability). Furthermore, the lack of lymphatic drainage in the tumor tissue makes it impossible to recapture these nanoparticles (enhanced retention). Thereby, nanoparticles could guide the Gef to the tumor tissue, leading to better anticancer efficacy. Besides, the nanoparticles enable us to overcome the major challenge in cancer therapy which is improving the amount of drug reaching the tumor in order to have an effective therapy while limiting the harm to healthy organs (K. Chen et al., 2018; Iyer et al., 2006).

There are a lot of techniques by which StNPs could be prepared, of these, nanoprecipitation is the most favorable due to its simplicity, reproducibility, and the use of eco-friendly chemicals (Chin et al., 2011; El-Sheikh, 2017). Soluble starch is cross-linked with sodium tripolyphosphate (TPP) via phosphorylation process to produce new materials such as monostarch monophosphate or distarch monophosphate, both display anionic character owing to the phosphate group (Carmona-Garcia et al., 2009; da Silva Miranda Sechi and Marques, 2017; Manoi and Rizvi, 2010). Many researchers prepared drug-loaded StNPs using harmful solvents to dissolve starch such as sodium hydroxide, urea, hydrochloric acid, or sulfuric acid (El-Naggar et al., 2015; Gutiérrez et al., 2020; Kim et al., 2017). Herein, we designed StNPs with an environment-benign solvent where hot water is used as the solvent for starch.

A full factorial design was implemented as a strategy to improve the synthesis of Gef-StNPs and to predict the optimum formula. The desired formula was characterized for drug content, entrapment efficiency (%EE), particle size (PS), transmission electron microscopy (TEM), scanning electron microscopy (SEM), and *in vitro* release studies. It was also subjected to physicochemical characterization using Fourier transform infrared spectroscopy (FTIR), X-ray diffraction (XRD), and differential scanning calorimetry (DSC) to examine the possible interaction between Gef and StNPs. *In vitro* cell line study illustrated that Gef-StNPs improved cellular drug uptake, inhibited cell growth, and induced apoptosis of A549 cells much more than the pure Gef.

In this piece of work, we exploited the nature's own nanoparticles to combat lung cancer, where starch was used as a nanocarrier for the cytotoxic drug "gefitinib" and the results were promising. The Gef-StNPs showed superior cellular drug uptake, cytotoxicity, and higher apoptotic population.

We investigated nanotechnology as a platform for delivery of gef into A549 human lung cancer cells. Furthermore, we utilized a quality by design approach to spot the optimum formula that is capable of localizing the gef inside the tumor cells. What distinguishes this work from the previous publications is the use of environment-benign solvent where water was used as the solvent for starch during the synthesis of starch nanoparticles, while all the reported methods in the fabrication of starch nanoparticles used harmful solvents like sodium hydroxide, hydrochloric acid, urea, and sulfuric acid.

2. Materials and methods

2.1. Materials

Soluble starch was provided by Starch and Glucose Company, Egypt. Gefitinib was kindly gifted by King Saud University, Saudi Arabia. Tween® 80 (polyethylene sorbitan monooleate) and Sodium tripolyphosphate (TPP) were obtained from Sigma–Aldrich Chemie GmbH (Germany). Phosphate buffer saline (FBS) was prepared from disodium hydrogen phosphate and potassium dihydrogen phosphate. An analytical grade absolute ethanol was used.

2.2. Method of Gef-StNPs preparation

Cross-linked starch nanoparticles were prepared by antisolvent nanoprecipitation technique as follows:

First, 250 mg soluble starch was dissolved in 10 mL water to form a paste. Next, 25 mL of boiling water was added to the paste and gave a cloudy or milky solution. Then, 100 mg Gef dissolved in 10 mL water containing different amounts of Tween® 80 (25 mg, 50 mg, 100 mg) was added to the starch solution. After that, 5 mL of water containing different amounts of TPP was added to the solution, and the solution was magnetically stirred for 1 h at a rate of 1500 rpm and temp. of 25 °C. The produced Gef-StNPs were precipitated by the addition of 50 mL ethanol. The obtained powder was centrifuged and washed twice with 80/20 ethanol/water to sweep the unreacted compounds and finally with ethanol. In the final stage, the nanoparticles were centrifuged for 1 h at 4500 rpm to isolate them. In the end, the supernatant was captured to determine the Gef encapsulation indirectly. The freeze-dried nanoparticle powders were kept in closed containers for further investigation.

2.3. Experimental design

Design of experiment (DOE) was used as a statistical tool to help study and understand the impact of the factors (alone and combined) on the responses (the product) and enable us to optimize the responses and analyze the studied factors. Studying of each factor is a tedious and time-consuming process. Thus, a full factorial design can overcome these drawbacks by optimizing the factors collectively at the same time, therefore reduces the total number

of experiments required for achieving the optimization of the process (Aref Shokri, 2019; Shokri, 2020, 2018). The main and interactive effects of the 2 experimentally studied factors "TPP and Tween" were investigated through the model equations designed by a three-level full factorial design. The predicted results from full factorial design model showed high values of R^2 revealing an agreement with the experimental data and reflecting the suitability of the full factorial design model (Arenas et al., 2007; Gottipati and Mishra, 2010; Seyed Shahabadi and Reyhani, 2014).

Three-level two-factor full factorial design (3^2) was proceeded utilizing the JMP® (version 16, SAS, USA) to study the effects of independent variables: TPP and Tween® 80 on the responses: PS, %EE, and %release to determine the optimum formula. JMP® analyzed the results to statistically explore the data and to visualize the findings.

2.4. %Entrapment efficiency (%EE)

1 mL of the supernatant was diluted to 10 mL methanol and the absorbance was measured spectrophotometrically (Shimadzu 1601; Shimadzu, Kyoto, Japan) at 250 nm using methanol as blank. The amount of free Gef in the supernatant was calculated. The amount of Gef entrapped was identified by subtracting the amount of free Gef in the supernatant from the initial amount of Gef (El-Naggar et al., 2015). The experiment was executed in triplicate for each formula and the average was calculated. The %EE is calculated as follows:

$$\%EE = (Total\,Gef - Free\,Gef)/Total\,Gef \times 100 \quad (1)$$

2.5. In vitro release study

The Gef release from the nanoformulations was conducted in triplicate by using type 2 USP apparatus. Accurately weighed Gef-StNPs equivalent to 5 mg Gef were placed in 900 mL FBS of pH 5, stirred at a rate of 100 rpm, and temperature of 37 °C. At predetermined time intervals (between 5 and 60 min) 4 mL sample was withdrawn and substituted with 4 mL fresh FBS. The amount of Gef released was determined by measuring the absorbance using a UV spectrophotometer (Shimadzu 1601; Shimadzu, Kyoto, Japan)) at 250 nm wavelength. The maximum %release was noted after 60 min. Therefore the %release of all the nanoformulations was recorded at this point of time.

2.6. Characterization

2.6.1. Fourier transform infrared (FTIR) spectroscopy

FTIR spectra of the pure Gef, starch, TPP, plain StNPs, and Gef-StNPs were recorded by Thermo Scientific Nicolet iS50 FTIR spectrometer, USA. KBr was mixed with the grounded dried sample and compressed into a pellet. FTIR spectra were obtained in the wavenumber range from 4000 cm^{-1} to 400 cm^{-1} (Liu et al., 2017).

2.6.2. Particle size (PS) and morphological characterization by DLS, transmission electron microscopy (TEM), and scanning electron microscopy (SEM)

All batches were evaluated for PS (nm) and polydispersity index (PDI) using the dynamic light scattering technique (Zetasizer Nano series Nano-ZS, Malvern Instruments, Malvern) at a scattering angle of 90^0 and a temperature of 25 °C.

The size and shape of the optimum formula were analyzed using TEM (JEOL, JEM-2100, Japan). One drop from diluted nanoparticles suspension was placed on a copper grid and allowed to dry. Morphological investigation of plain StNPs and Gef-StNPs was done by using SEM (Quanta FEG-250 SEM instrument, USA) (Xia et al., 2017).

2.6.3. Thermal analysis

2.6.3.1. Differential scanning calorimetry (DSC). DSC identifies the chemical interaction of Gef and StNPs. DSC measurements were carried out by LABSYS evo Setaram, France. 2–10 mg samples were laid on aluminum pans and sealed. The probes were exposed to temperatures from 25 to 250 °C at a rate of 10 °C/min under an atmosphere of nitrogen (Liu et al., 2017).

2.6.3.2. X-ray diffraction (XRD). XRD analysis was employed to detect the crystallinity of the pure Gef and the Gef-StNPs, which was conducted using Bruker D8 discover diffractometer with copper sealed tube X-ray source producing Cu-Kα radiation at a wavelength of 1.5406 A^0. The relative intensity data were collected over the 2θ range of 5–80^0 (Phillip Lee et al., 2009).

2.6.4. In vitro cytotoxicity

2.6.4.1. Cell viability assay. Yellow MTT (3-(4, 5-Dimethylthiazol-2-yl)-2, 5- diphenyltetrazolium bromide, a tetrazole) is reduced to purple formazan in the mitochondria of living cells. This reduction occurs only with active mitochondrial reductase enzymes, and therefore conversion is a key indicator of the number of viable cells.

Cytotoxicity was determined in a cell line (A549) non-small cell lung cancer (Nawah-Scientific, Cairo, Egypt). Cells were grown in a DMEM medium supplemented with 10 % FBS, 100 units/mL of penicillin, and 100 mg/mL of streptomycin(Garizo et al., 2021). Cultures were maintained in a humidified atmosphere with 5 % CO_2 at 37 °C.

Each sample was diluted in DMEM complete media at 37 °C to give a stock solution.

10 Concentrations of twofold serial dilutions were conducted.

Briefly, Confluent monolayers of cells were grown in 96 well-microtiter plates for 24 hrs. Cells were incubated with various concentrations of the test samples in triplicate at 37 °C in a CO_2 environment for 72 hrs. After that, gently added 20 µL 5 mg/mL MTT to each well and incubated at 37 °C for 4 hrs. Then, the media was carefully removed followed by the addition of 150 µL MTT solvent. Covered with tinfoil and cells agitated on an orbital shaker for 15 min. Finally, the OD was measured at 570 nm in a microplate reader (BMGLABTECH®FLUOstar Omega, Germany).

2.6.4.2. Evaluation of apoptosis by Annexin-V/PI staining assay. Flow cytometry assesses the apoptotic pathways using Annexin V-FITC apoptosis detection kit (Abcam Inc., Cambridge Science Park, Cambridge, UK) coupled with 2 fluorescent channels flow cytometry. After treatment with test compounds for 72 hrs and doxorubicin (10 µM) for 48 hrs as a positive control, cells (10^5 cells) are collected by trypsinization and washed twice with ice-cold PBS (pH 7.4). Then, cells were incubated with 0.5 mL of Annexin V-FITC/PI solution for 30 min in dark at room temperature. After staining, cells were injected via ACEA Novocyte™ flow cytometer (ACEA Biosciences Inc., San Diego, CA, USA) and analyzed for FITC and PI (Wang et al., 2010) fluorescent signals using FL1 and FL2 detector, respectively ($\lambda_{ex/em}$ 488/530 nm for FITC and $\lambda_{ex/em}$ 535/617 nm for PI). For each sample, 12,000 events were acquired and positive FITC and/or PI cells were quantified by quadrant analysis and calculated using ACEA NovoExpress™ software (ACEA Biosciences Inc., San Diego, CA, USA).

2.6.4.3. Cellular drug uptake. Non-small cell lung cancer A549 cell lines maintained in DMEM/RPMI-1640 media supplemented with 100 mg/mL of streptomycin, 100 units/mL of penicillin, and 10 % of heat-inactivated fetal bovine serum in humidified, 5 % (v/v) CO_2 atmosphere at 37 °C. Cells were seeded in a T25 flask (Greiner bio-one, Germany) for 24 hrs. Then, cells were treated with fresh media containing the predetermined drug concentration. Cells at

a confluence of 80 % were harvested using trypsin/EDTA after the requested time of incubation. Then, the pellet was obtained using a cooling centrifuge.

HPLC analysis:

a) Standard preparation: Stock solution of Gef in methanol was prepared then serial dilution to obtain the concentration of (0.1, 0.2, 0.4, 0.6, 0.8, 1 μg/mL), filtered using 0.22 μm syringe filter then 100 μL were injected.

b) Sample preparation: 0.5 mL Acetonitrile added to each sample then vortexed for 1 min then sonicated for 30 min then centrifuged for 15 min at 15,000 rpm, filtered using 0.22 μm Nylon syringe filter then 100 μL was injected.

3. Results and discussion

3.1. DOE: Effect of TPP and Tween® 80 on the PS (nm), %EE, and % release

DOE facilitates the simultaneous assessment of the impact of TPP and Tween® 80 as well as their actual significance on the selected responses. Table 1 describes the full factorial design. Investigation of the effect of TPP and Tween® 80 revealed the significant effect of TPP on PS (P-value = 0.0002), %EE (P-value = 0.0012), and %release (P-value = 0.0003) (Fig. 1 a, b, and c. . Similarly, Tween® 80 had statistically significant effect on PS (P-value = 0.0004), %EE (P-value = 0.0020), and %release (P-value = 0.0007), (Fig. 1 a, b, and c). Moreover, TPP and Tween® 80 had only a linear model, the P-values for TPP and Tween® 80 were 0.00025 and 0.00042, respectively. The interactive effect of TPP and Tween®80 was insignificant (P-value = 0.43107) Fig. 2. The experimental data had a high degree of correlation with the predicted response, the PS actual vs the predicted plot had an R^2 of 0.97 and a P-value of 0.0003, the %EE actual vs the predicted plot had an R^2 of 0.94 and a P-value of 0.0017, and eventually the %release actual vs the predicted plot had an R^2 of 0.97 and a P-value of 0.0004 (Figs. 3a-3c). The statistical factorial approach optimized the responses using the desirability function. The desirability is a mathematical method used to spot the optimized formulation. The optimization was set for minimum PS, maximum %EE, and maximum %release. From factorial design we have selected F8 (TPP = 25 mg, and Tween®80 = 100 mg) as the optimum formula (PS = 76 nm, %EE = 93.7 %, and %release = 99.3 %) with desirability = 0.948 (Fig. 4.).

3.1.1. Effect of TPP on PS, %EE, and %release

It is apparent from the cell plot in Fig. 5. that the PS ranges from 76 to 309 nm and manifests an upward trend with the rise in TPP. An increase in TPP enlarges the PS (El-Naggar et al., 2015). At TPP of 25 mg (F2, F8, F9), the mean PS was 125 nm. While at TPP of 50 mg (F3, F4, F6), the mean PS rose to 179 nm, and at TPP of 100 mg (F1, F5, F7), the mean PS skyrocketed to 259 nm, Fig. 6(a). The data dictate that the PS booms with TPP elevation.

The %EE ranges from 57.4 to 93.7 %, Fig. 6(b). shows a downward trend with the jump in TPP. At TPP 25 mg (F2, F8, F9), the mean %EE was 87%, while at TPP 50 mg (F3, F4, F6), the mean % EE dropped to 75%, and at TPP 100 mg (F1, F5, F7), the mean %EE sank to 65%, Fig. 6(b). The data reveal a %EE plunge with the rise in TPP.

It is crystal clear that higher TPP enlarges the PS, and the PS has a great influence on Gef entrapment, where the smallest particles have a large surface area, and hence catch more drug inside the nano-truck, while large particles unable to enter the core of StNPs. Therefore, a significant enhancement in Gef encapsulation was observed with the lowest TPP concentration.

Finally, TPP shows a great impact on Gef release from StNPs. % Release ranges from 61.7 to 99.3 %, Fig. 6(c). shows a downward trend with increasing TPP. At TPP 25 mg (F2, F8, F9), the mean %release was 90%, while at TPP 50 mg (F3, F4, F6), the mean %release fell to 81%, and at TPP 100 mg (F1, F5, F7), the mean %release shrank to 68%. The data conclude that the %release contracted with higher TPP. This shrinkage illustrates that lower TPP concentration led to small PS (large surface area), and hence the particles dissolve easily. Furthermore, soluble starch is entirely cross-linked at low TPP and results in a high molecular weight structure with wide pores, and therefore high release. Conversely, higher TPP leads to a highly cross-linked starch network, which consequently hinders Gef release.

The response surface plot of TPP effect on PS (nm), %EE and %release is shown in (Figs. 7a-7c).

3.1.2. Effect of Tween®80 on PS, %EE, and %release

As depicted in Fig. 2. Tween® 80 had a significant effect on PS, % EE, and %release.

PS shows a downward trend with increasing Tween® 80 concentration (Sadeghi et al., 2017). At Tween® 80 of 25 mg (F1, F4, F9), the mean PS was 245 nm. While at Tween® 80 of 50 mg (F2, F3, F5), the mean PS declined to 194 nm, and at Tween® 80 of 100 mg (F6, F7, F8), the mean PS Plunged to 124 nm, Fig. 8(a). Therefore, higher Tween® 80 concentration leads to smaller PS, because surfactant limits the growth of StNPs. Low Tween® 80 (25 mg) is unable to entirely coat the droplets' surface area. Consequently, the droplets stick together, thereby producing large particles with a small surface area. In a nutshell, Tween® 80 acts as a stabilizing agent during the formation of nanoparticles and inhibits crystal growth. A Similar trend of Tween® 80 impact on PS was reported with gold nanoparticles and chitosan-coated alginate nanoparticles (Scolari et al., 2019; Suchomel et al., 2018).

In terms of the %EE, it's proportional to Tween® 80 concentration (Chin et al., 2014). At Tween® 80 of 25 mg (F1, F4, F9), the mean %EE was 67%. While at Tween® 80 of 50 mg (F2, F3, F5),

Table 1
Full factorial design run matrix and the obtained responses: TPP and Tween are the studied factors, while the PS, the %EE, and the %Release are the responses.

Full factorial design					
Formula	**Independent variable**		**Dependent variables (Responses)**		
	TPP	**Tween**	**PS (nm)**	**%EE**	**%Release**
F1	**100**	**25**	**309**	**57.4**	**61.7**
F2	**25**	**50**	**117**	**84.9**	**86.1**
F3	**50**	**50**	**197**	**74.1**	**81.8**
F4	**50**	**25**	**245**	**63.6**	**69**
F5	**100**	**50**	**267**	**59.4**	**64.9**
F6	**50**	**100**	**94**	**86.2**	**91.7**
F7	**100**	**100**	**202**	**76.8**	**77.2**
F8	**25**	**100**	**76**	**93.7**	**99.3**
F9	**25**	**25**	**182**	**81.4**	**84.1**

a

Term	Estimate	Std Error	t Ratio	Prob> [t]
Intercept	188.43	6.02	31.28	<0.0001
TPP(25,100)	66.34	7.18	9.24	0.0002
Tween(25,100)	-59.33	7.18	-8.26	0.0004
TPP*Tween	1.17	8.56	0.14	0.8965

Fig. 1a. Parameter estimates display the significant effect of tpp and tween on the ps (p-value < 0.05), while the interactive effect was insignificant (P-value > 0.05).

b

Term	Estimate	Std Error	t Ratio	Prob> [t]
Intercept	75.14	1.33	56.67	<0.0001
TPP(25,100)	-10.39	1.58	-6.57	0.0012
Tween(25,100)	9.30	1.58	5.89	0.0020
TPP*Tween	1.61	1.88	0.86	0.4311

Fig. 1b. Parameter estimates display the significant effect of tpp and tween on the %ee (p-value < 0.05), while the interactive effect was insignificant (P-value > 0.05).

c

Term	Estimate	Std Error	t Ratio	Prob> [t]
Intercept	79.32	0.99	80.15	<0.0001
TPP(25,100)	-10.8	1.18	-9.15	0.0003
Tween(25,100)	8.86	1.18	7.51	0.0007
TPP*Tween	-0.29	1.41	-0.21	0.8451

Fig. 1c. Parameter estimates display the significant effect of tpp and tween on the %release (p-value < 0.05), while the interactive effect was insignificant (P-value > 0.05).

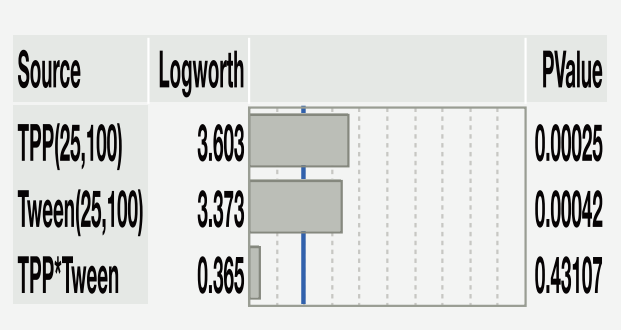

Fig. 2. Pareto chart displays the linear model (TPP and Tween 80 had significant effect (P-value < 0.05) on PS, %EE and %Release, but the interactive effect (quadratic) wasn't significant (P-value > 0.05).

the mean %EE climbed to 73%, and at Tween® 80 of 100 mg (F6, F7, F8), the mean %EE spiked to 86%, Fig. 8(b). This reflects the great influence of PS on the Gef encapsulation into StNPs, lower PS produced at higher Tween® 80 concentration has a large surface area capable of capturing more drug in the core of nanoparticles and increasing the efficiency of Gef loading.

When it comes to %release, it jumped up with a higher Tween® 80 concentration. At Tween® 80 of 25 mg (F1, F4, F9), the mean % release was 72%. While at Tween® 80 of 50 mg (F2, F3, F5), the mean %release hiked to 78%, and at Tween® 80 of 100 mg (F6, F7, F8), the mean %release peaked at 89%, Fig. 8(c). The %release was higher with the highest Tween® 80, this is due to small PS, large surface area, and high energy state which increases the dissolution of the particles and expands the hydrophilic character and the wettability of the nanoformulations.

Figs. 9a- 9c. display the surface plot.

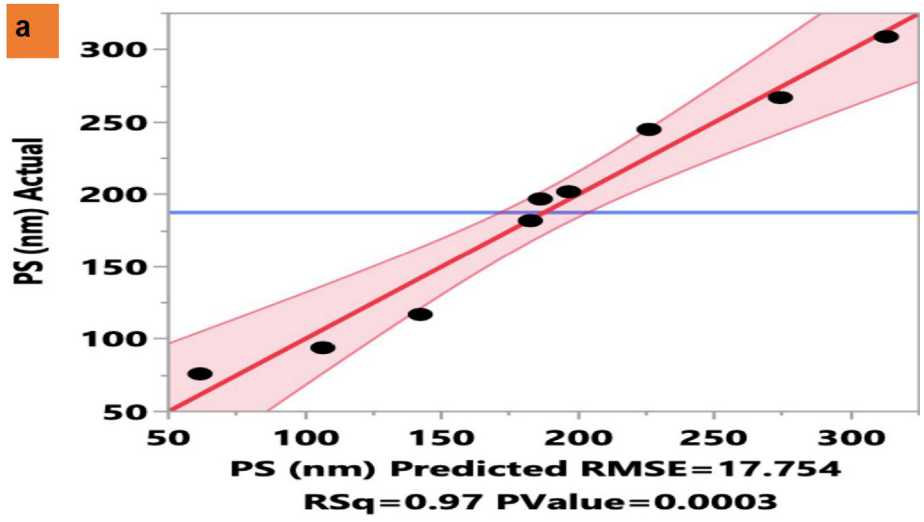

Fig. 3a. Experimental values obtained from the 9 nanoformulations were very close to the predicted values.

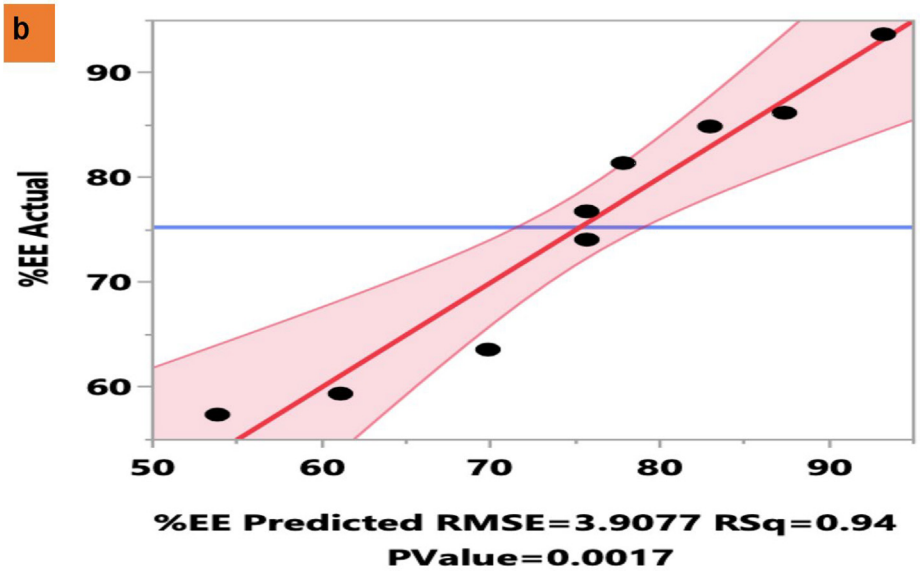

Fig. 3b. Experimental values obtained from the 9 nanoformulations were very close to the predicted values.

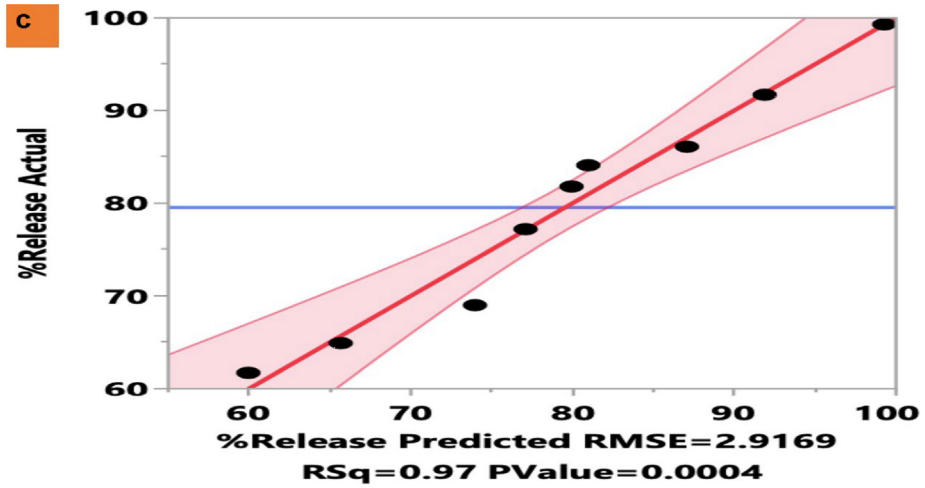

Fig. 3c. Experimental values obtained from the 9 nanoformulations were very close to the predicted values.

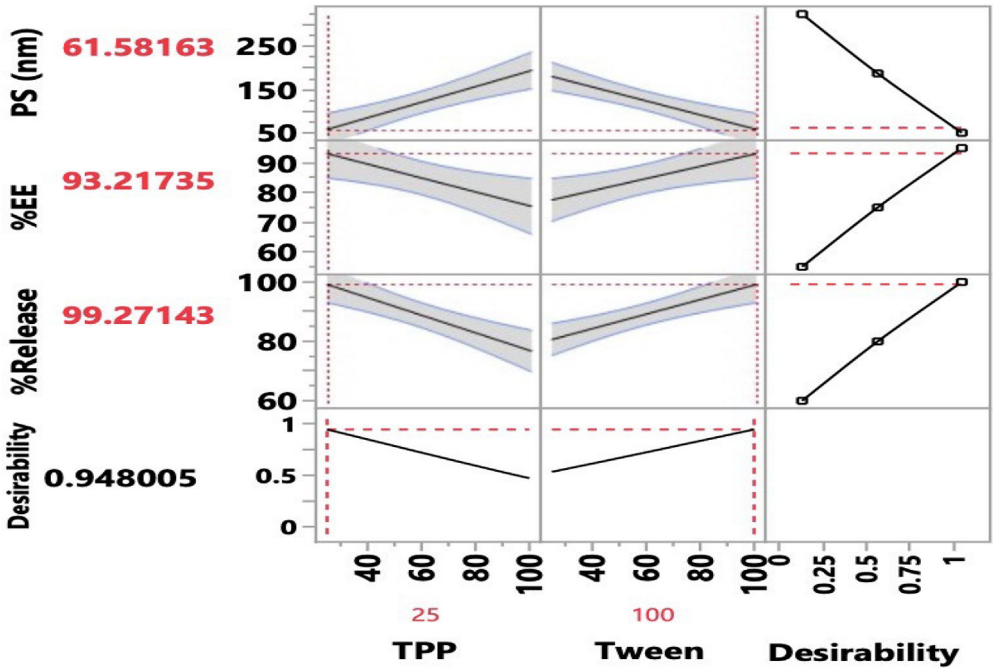

Fig. 4. The prediction profiler with desirability function (predicts the optimal conc. of TPP and Tween for the 3 dependent variables).

Figs. 10a-10c. display the impact of TPP and Tween® 80 on the PS, the %EE and the %release, respectively.

(Figs. 11a-11f.) display theimpact of TPP and Tween on the PS (nm), %EE and the %release, respectively via the heatmap.

3.2. Drug encapsulation (%EE) by the cross-linked starch nanoparticles

The entrapment efficiency of Gef in the 9 nanoformulations were determined as illustrated in Fig. 12.

The average %EE ranges from 57 to 94%.

3.3. In vitro release study

We conducted the *in vitro* release study to predict and compare the bioavailability of the pure Gef and Gef-StNPs. It is carried out in FBS at pH of 5 and temperature of 37 °C.

As shown in Figs. 13 and 14, the pure Gef has the lowest %release of 40 % after 60 min, while all the nanoformulations have a much higher %release ranging from 62 to 99% at the same period.

3.4. FTIR spectroscopy

The FTIR spectra of the pure Gef, soluble starch, TPP, plain StNPs, and Gef-StNPs are shown in (Figs. 15a-15e).

Gef shows the following: a sharp peak at 3399.61 cm^{-1} (Gidwani et al., 2018) that was assigned to the secondary amine group, N—H bending vibration from 1532.66 to 1625.01 cm^{-1}, C–Cl peaks in the region of 545.08 – 774.65 cm^{-1}, C–F peaks in the region of 1028.72 to 1397.68 cm^{-1}, C—O peaks at 1110.18 cm^{-1}, –C═N peak at 1902.9 cm^{-1}. Peaks at a region of 654.56 to 911.75 are characteristic of the aromatic region (900–650 cm^{-1}) and = C—H peak at 3100.14 cm^{-1}.

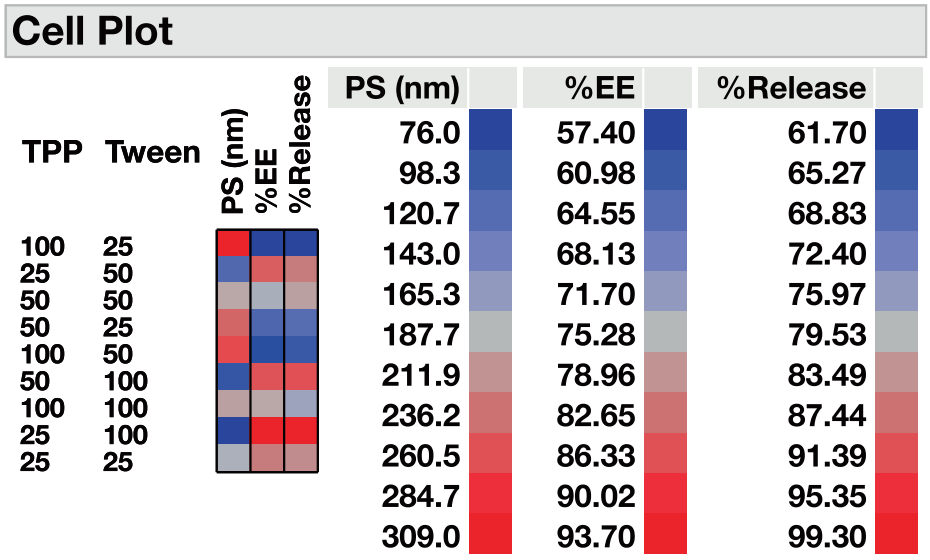

Fig. 5. The cell plot shows that the PS ranges from 76 to 309 nm, the %EE ranges from 57.4 to 93.7 % and the %Release ranges from 61.7 to 99.3 %.

Starch shows the following: broad band at 3384.96 cm^{-1} is an indicator of –OH stretching vibration (Lopez-Silva et al., 2021).

The region between 929.63 and 1240.82 cm^{-1} is assigned to the stretching vibration of C—C and C—O. Peaks at 2927.04 to 1083.08 cm^{-1} were assigned to the C—H stretching of glucose units. Peaks at 609.2 to 1375.2 are the fingerprint region of C—C and C—O bonds in starch. The characteristic peak of C—O—C ring vibration in starch is located at 765.76 cm^{-1}.

Plain StNPs show the following: broad band at 3421.7 cm^{-1} (–OH stretching vibration), peak at 2922.79 due to C—H stretching vibration. C—O peak at 1105.99 cm^{-1}.

Gef-StNPs show a broad band at 3400.03 cm^{-1} attributed to –OH stretching vibration. The peak at 2923.05 cm^{-1} is due to C—H stretching vibration. The peak at 1108.87 cm^{-1} due to C—O.

Peaks of Gef in the aromatic region disappeared reflecting Gef encapsulation and the high similarity between plain StNPs and Gef-StNPs indicates the high efficiency of Gef encapsulation inside StNPs. Absence of characteristic peaks of Gef due to its encapsulation.

3.5. Particle size and morphology analysis by DLS, TEM and SEM

PS analysis is used to understand dispersion and aggregation. Large particles tend to clump together compared to small particles, thereby resulting in a deposition. PDI is an indicator of nanoparticle homogeneity. Homogeneous nanoparticle dispersion has a PDI value that approaches zero, while a PDI value > 0.5 reflects high heterogeneity. The results from DLS reveal that the 9 batches have PS range from 76 to 309 nm, Figs. 16 and 17, and PDI range from 0.094 to 0.446 (PDI < 0.5) indicating uniformity of Gef-StNPs. Therefore, soluble starch as a biopolymer can entrap Gef at a nano-range. The PS determined by DLS was larger when compared with TEM images, due to the analysis occurring in solution in case of DLS and the particles are vulnerable to agglomerate and hence increasing PS. While TEM measurement represents a dried layer of nanoparticles on a TEM grid and there is no likelihood to aggregate.

The morphology of plain StNPs, and Gef-StNPs by SEM and TEM Fig. 18. TEM micrograph Fig. 18. displayed that Gef-StNPs have narrow PS distribution (Dong et al., 2020), ranging from 7.02 nm to 45.7 nm with an average size of 28.7 nm, which as anticipated was smaller than the DLS measurement.

The SEM images of plain StNPs and Gef-StNPs in Fig. 18. showed porous structures possessing open and filled channels (Thi et al., 2021), these porous structures are suitable for entrapping Gef inside the cavities. The SEM micrographs showed no notable change in the surface morphology of plain StNPs and Gef-StNPs confirming the encapsulation of Gef inside the StNPs.

3.6. Thermal analysis

3.6.1. DSC

The thermogram of Gef, plain StNPs, and Gef-StNPs showed in Fig. 19. The DSC thermogram of pure Gef exhibits a sharp endothermic peak at 195.067 °C "the melting temperature" (Nayek et al., 2021a, 2021b) with a melting temperature range of 184.54 – 236.90 °C, and the heat of fusion (ΔH) was 166.597 (J/g) implying the crystalline nature of Gef.

DSC thermogram of plain StNPs displays a sharp endothermic melting temperature at 99.858 °C with a melting temperature range of 44.56 to 183.99 °C, and the heat of melting (ΔH) was 365.873 (J/g). The second endothermic peak observed at 215.864 °C with the heat of melting equal to 1.615 (J/g) was ascribed to the degradation temperature value of plain StNPs.

DSC thermogram of Gef-StNPs reveals a sharp endothermic peak at 89.875 °C with a melting temperature range of 39.72 and 165.55 °C, and the enthalpy (ΔH) was 234.116 (J/g). The second endothermic peak observed at 183.499 °C with the heat of melting equal to 3.013 (J/g) was attributed to the degradation temperature value of Gef-StNPs. The characteristic peak of Gef faded away from the Gef-StNPs, indicating the complete dispersion of Gef in the StNPs. Moreover, this thermal analysis proves the thermal stability of Gef-StNPs at high temperatures.

3.6.2. XRD

The diffractogram of Gef (Figs. 20a-20c) showed characteristic sharp diffraction peaks at 2θ values of 19.348^0, 20.655^0, 22.523^0, 24.230^0, 26.389^0, 28.616^0, 35.978^0, 42.124^0, and 49.903^0. Similar

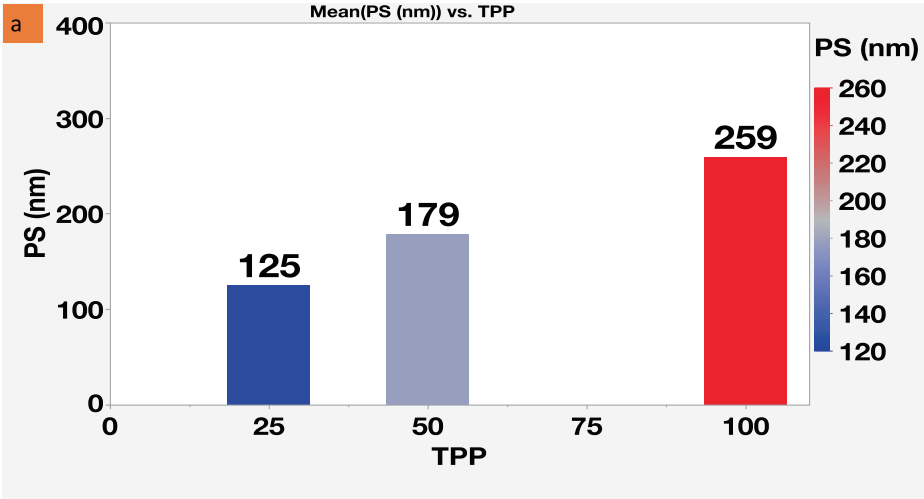

Fig. 6a. Bar graph displays that the mean PS increases with higher TPP levels.

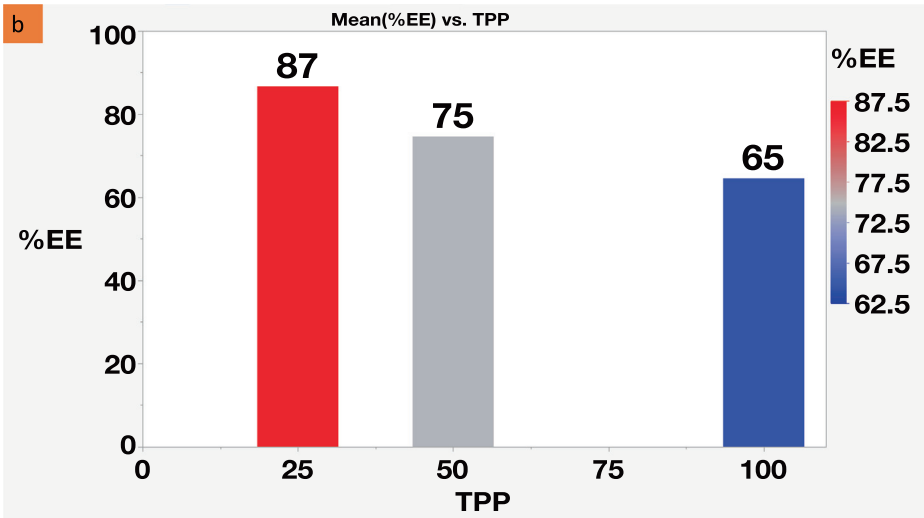

Fig. 6b. Bar graph displays that the mean %EE decreases with higher TPP levels.

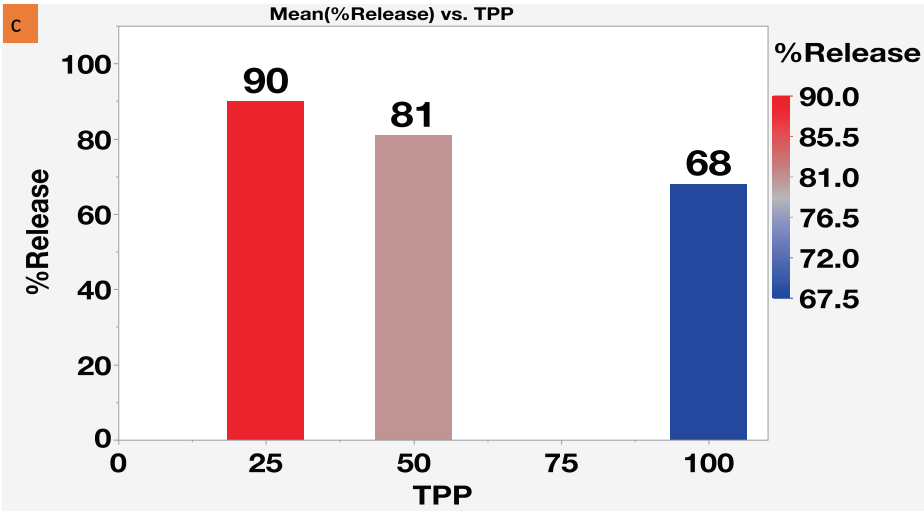

Fig. 6c. Bar graph displays that the mean %Release decreases with higher TPP levels.

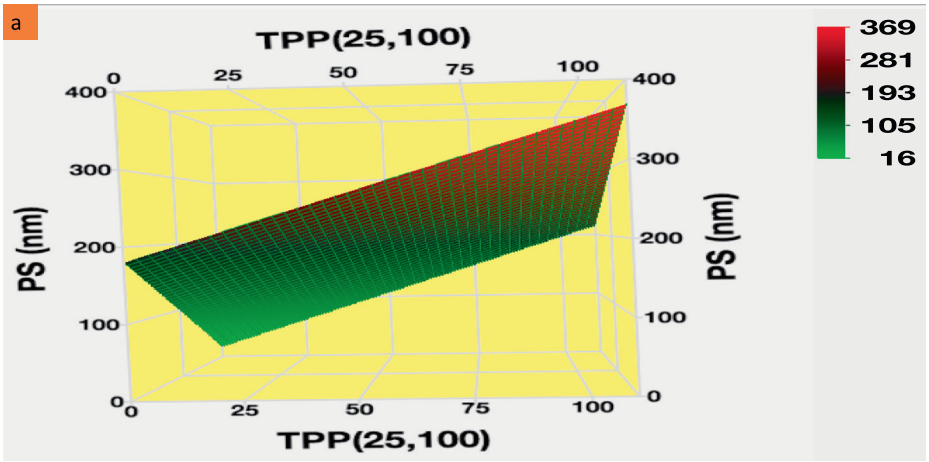

Fig. 7a. Response Surface plot demonstrates that higher TPP increases the PS.

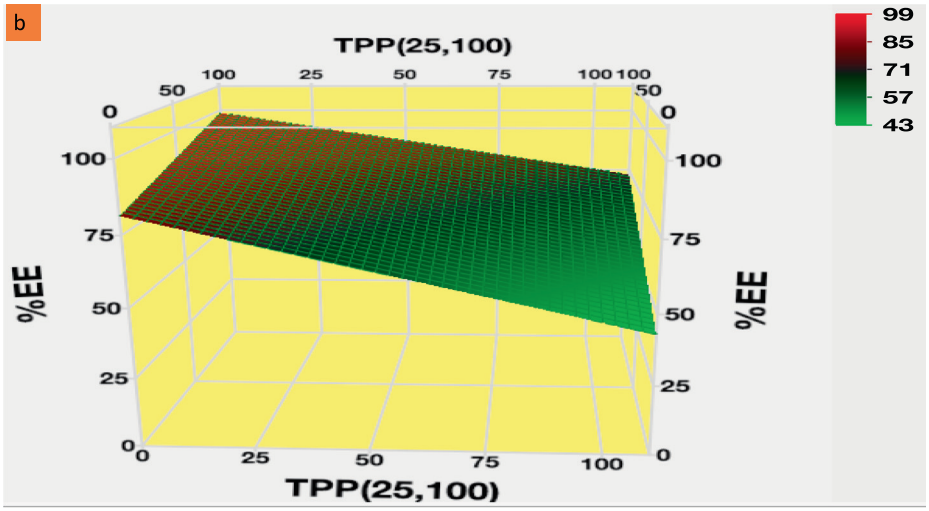

Fig. 7b. Response Surface plot demonstrates that higher TPP decreases the %EE.

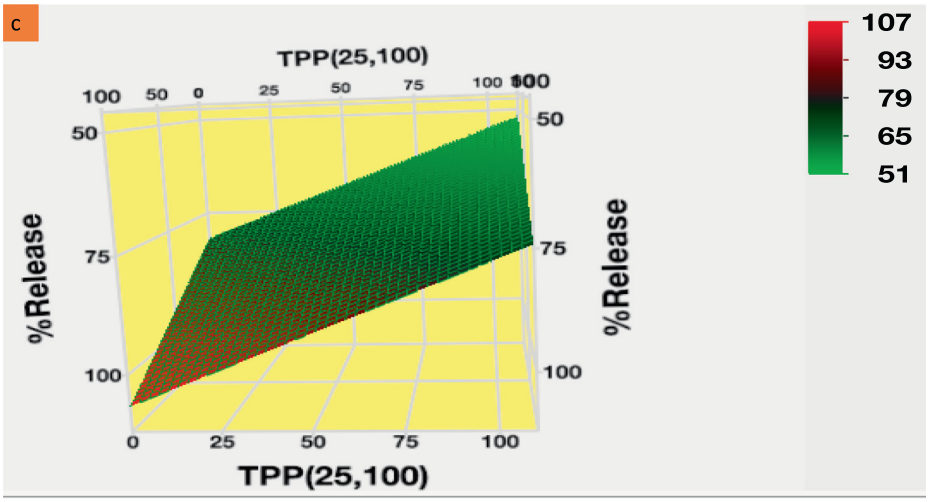

Fig. 7c. Response Surface plot demonstrates that higher TPP decreases the %Release.

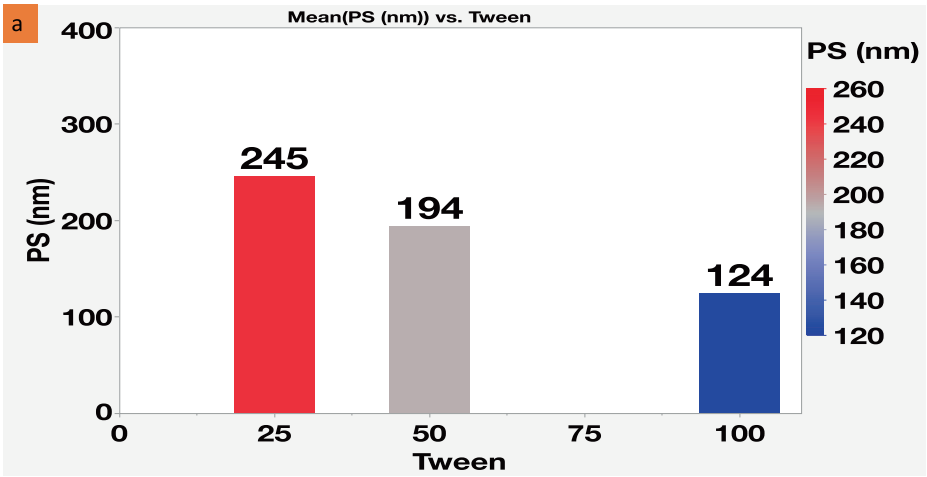

Fig. 8a. BAR graph displays that the mean PS decreases with higher Tween levels.

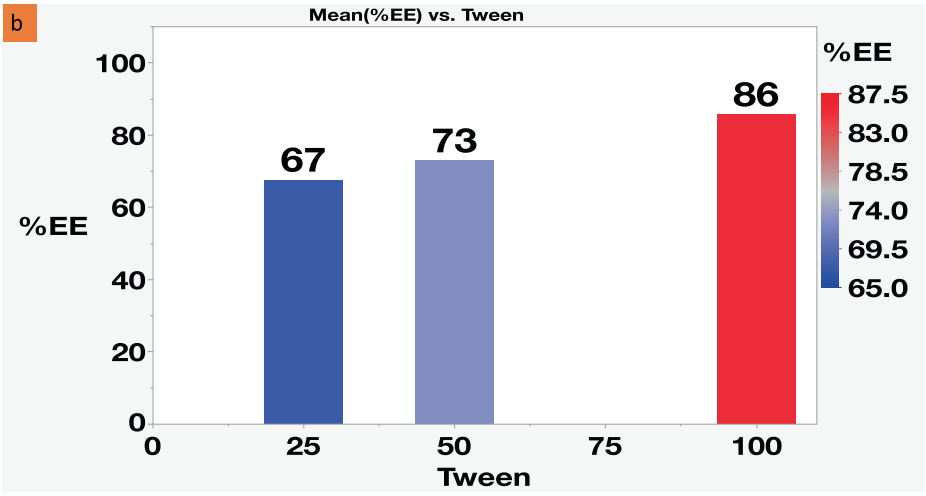

Fig. 8b. Bar graph displays that the mean %EE increases with higher Tween levels.

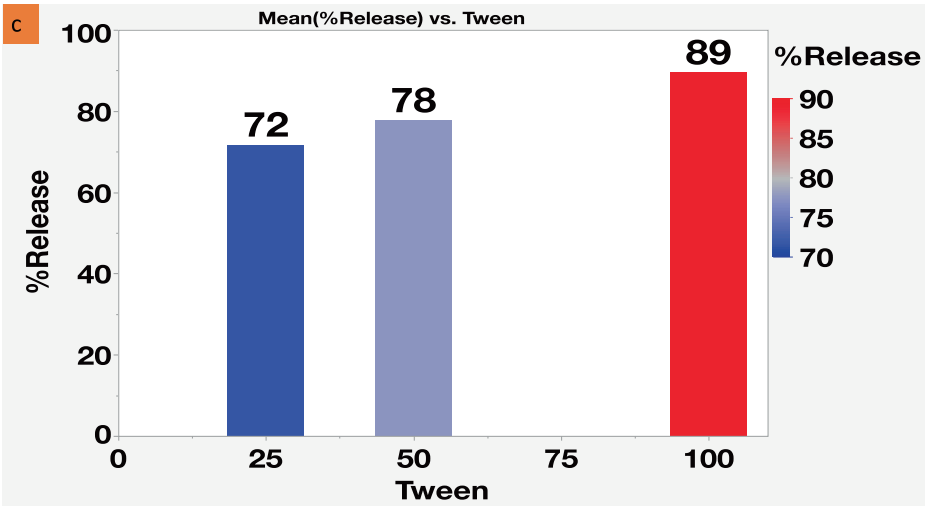

Fig. 8c. Bar graph displays that the mean %Release increases with higher Tween levels.

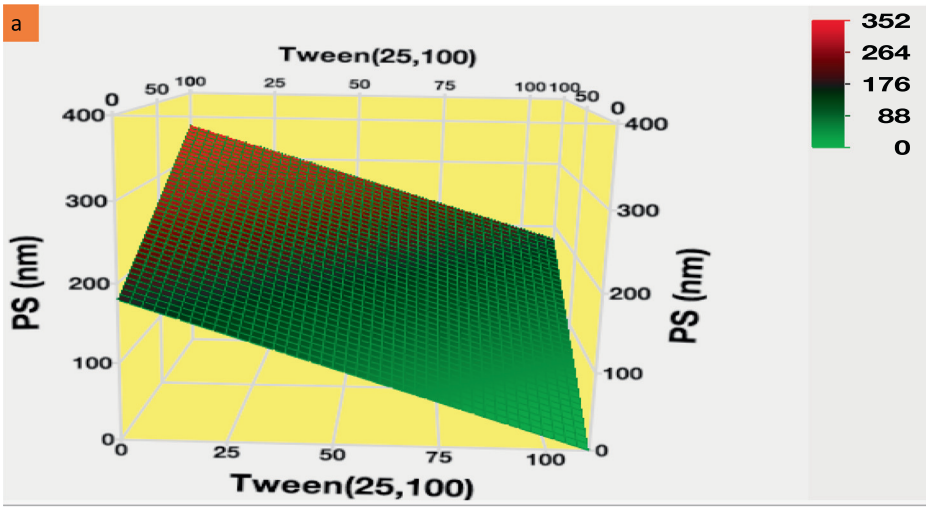

Fig. 9a. Response Surface plot demonstrates that higher Tween decreases the PS.

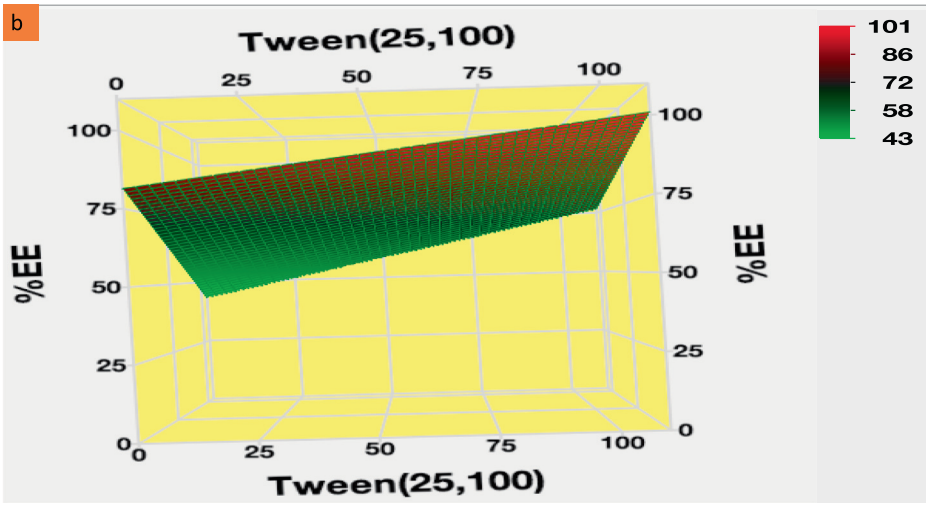

Fig. 9b. Response Surface plot demonstrates that higher Tween increases the %EE.

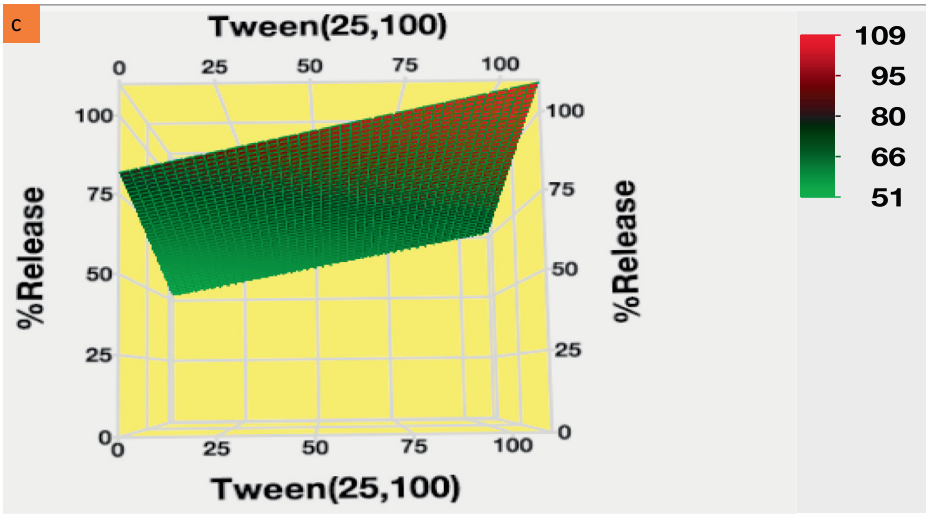

Fig. 9c. Response Surface plot demonstrates that higher Tween increases the %Release.

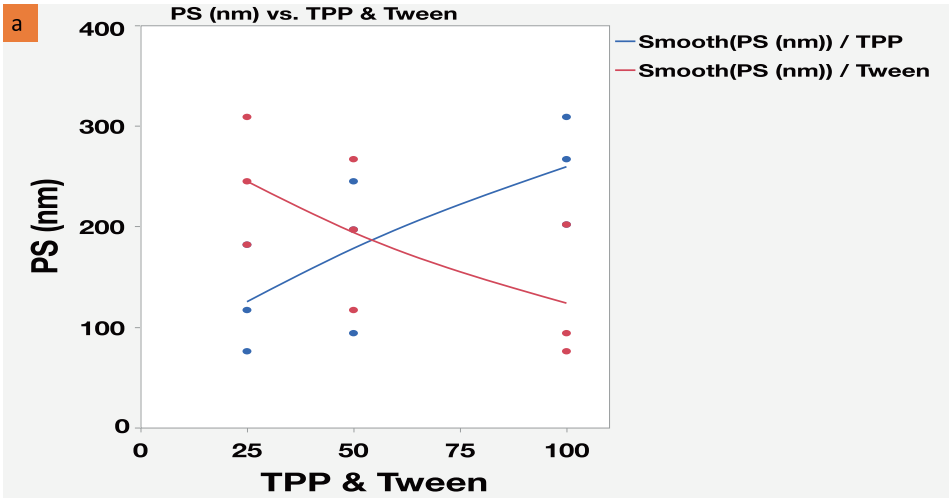

Fig. 10a. Graph shows a rise in PS with higher TPP conc. and a decline in PS with higher Tween concentrations.

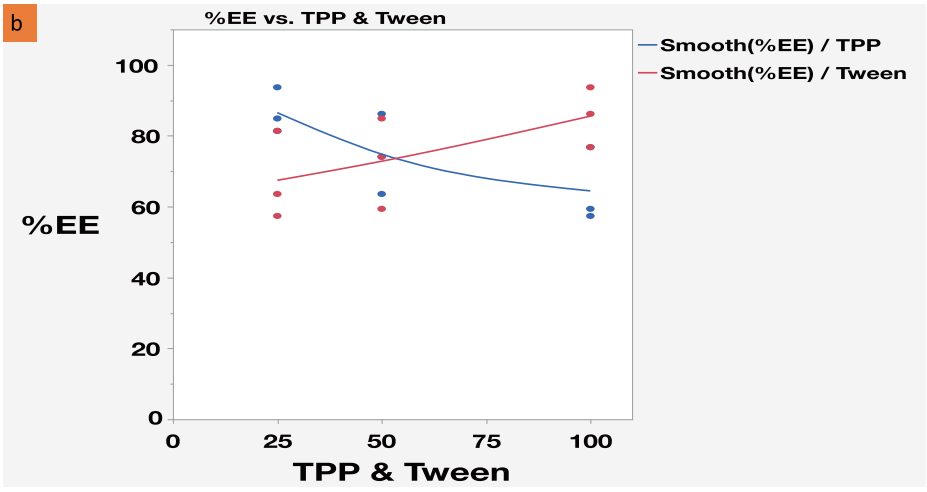

Fig. 10b. Graph shows a decline in %EE with higher TPP conc. and a rise in %EE with higher Tween concentrations.

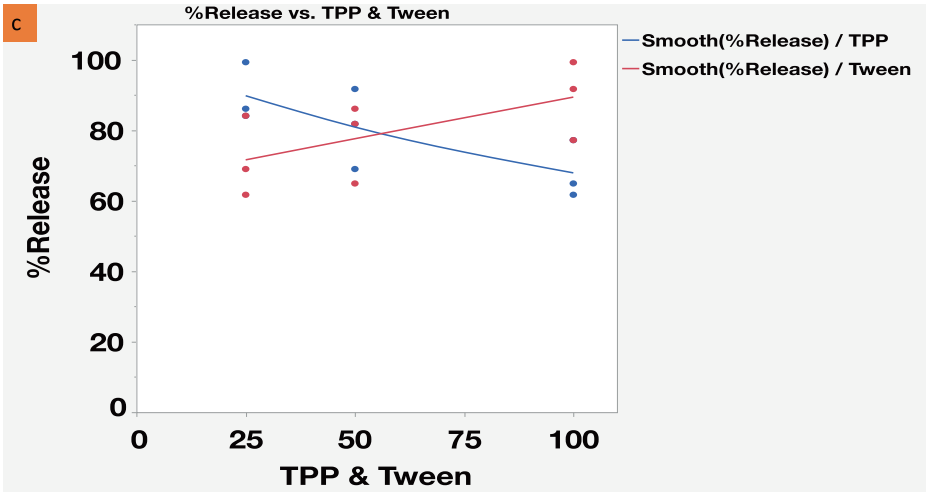

Fig. 10c. Graph shows a decline in %Release with higher TPP conc. and a rise in %Release with higher Tween concentrations.

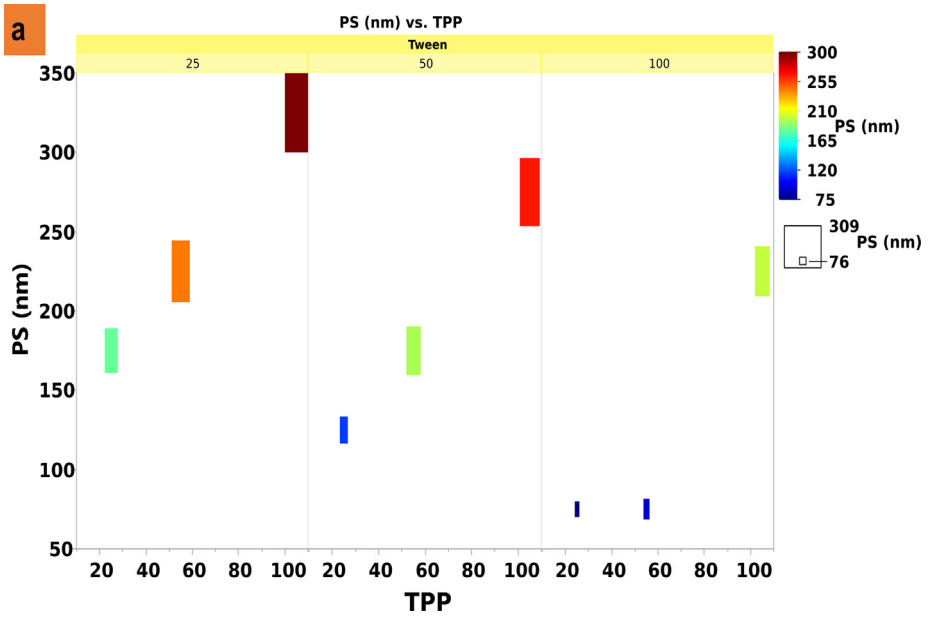

Fig. 11a. Heatmap shows the impact of TPP on the PS, revealing that higher TPP increases the PS.

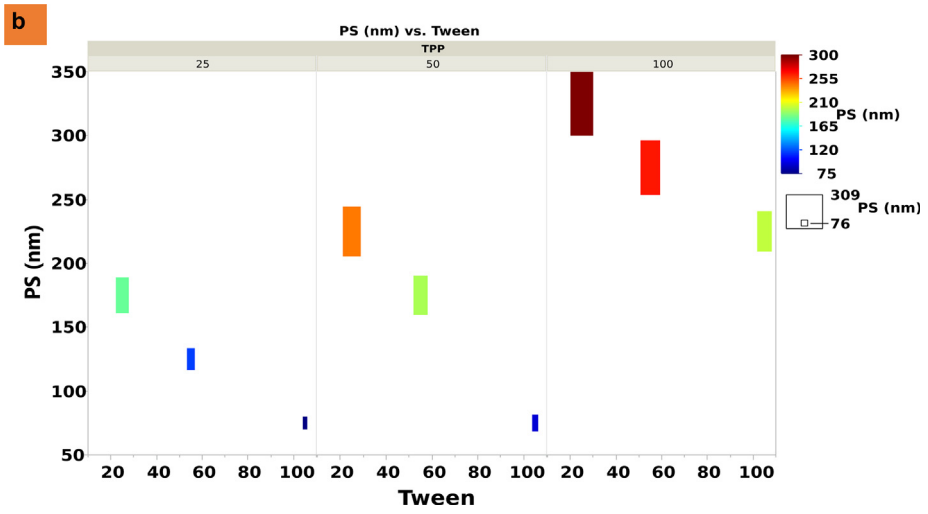

Fig. 11b. Heatmap shows the impact of Tween on the PS, revealing that higher Tween decreases the PS.

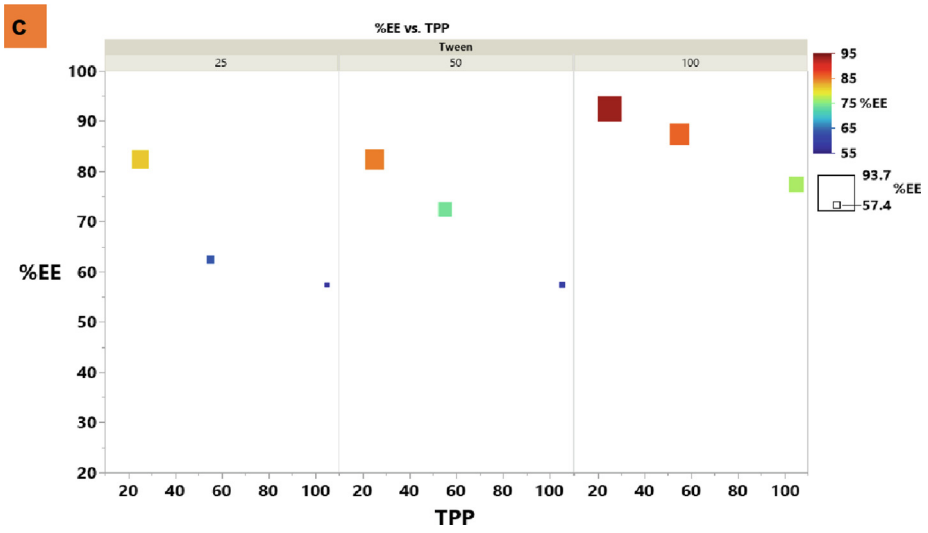

Fig. 11c. Heatmap shows the impact of TPP on the %EE, revealing that higher TPP decreases the %EE.

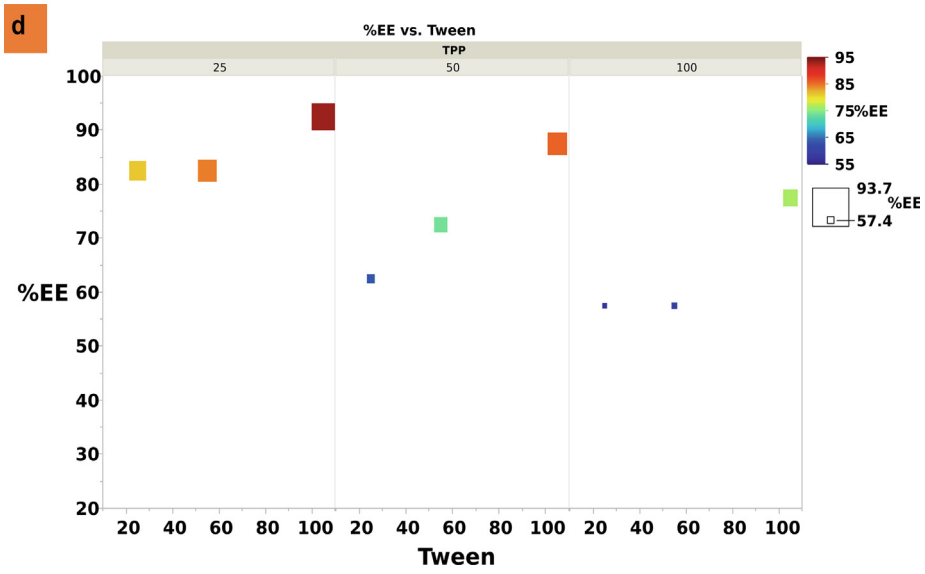

Fig. 11d. Heatmap shows the impact of Tween on the %EE, revealing that higher Tween increases the %EE.

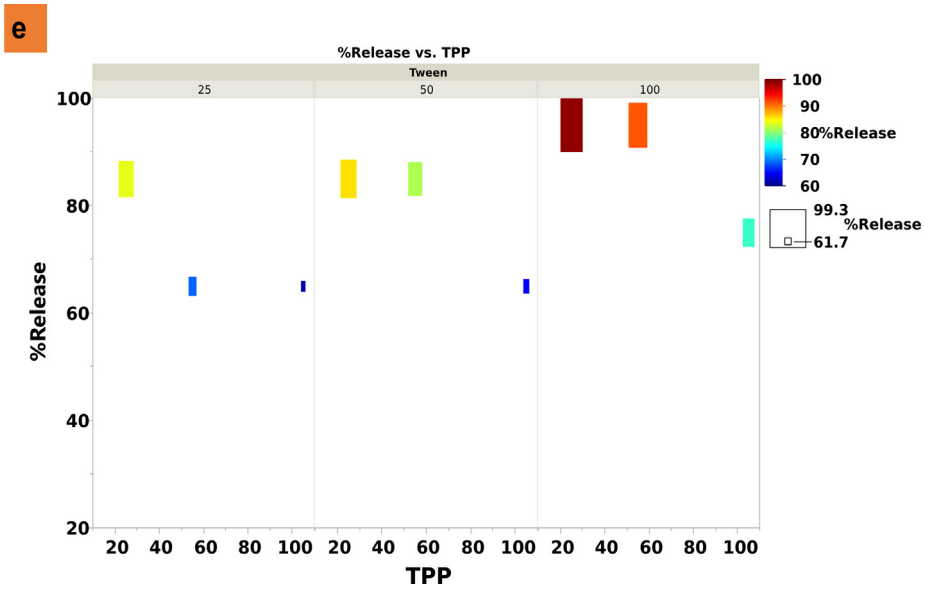

Fig. 11e. Heatmap shows the impact of TPP on the %Release, revealing that higher TPP decreases the %Release.

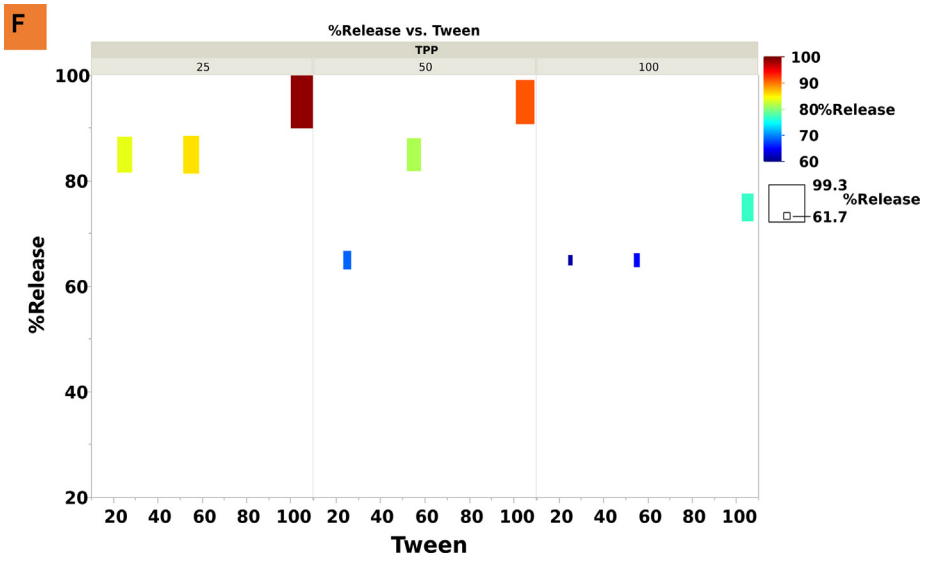

Fig. 11f. Heatmap shows the impact of Tween on the %Release, revealing that higher Tween increases the %Release.

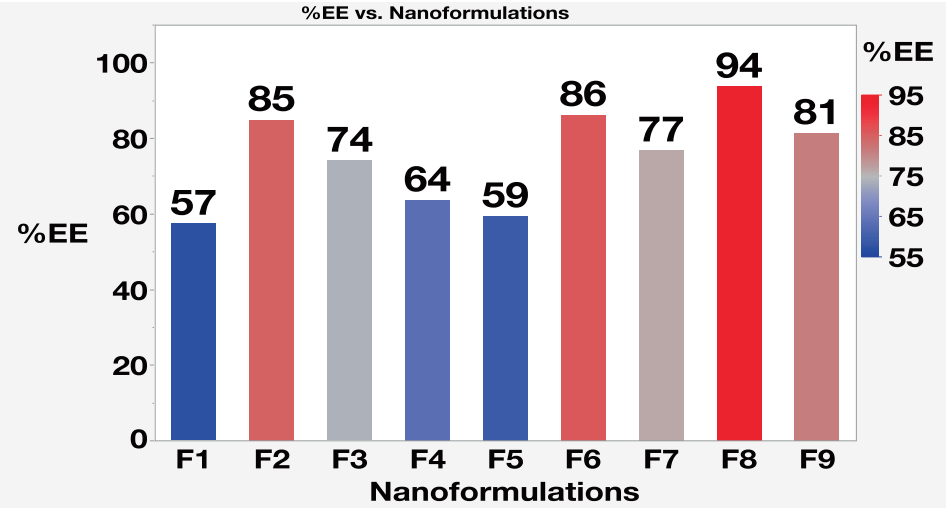

Fig. 12. The %EE of the 9 nanoformulations. The data expressed as the mean %EE (The optimized nanoformula is discriminated by red color).

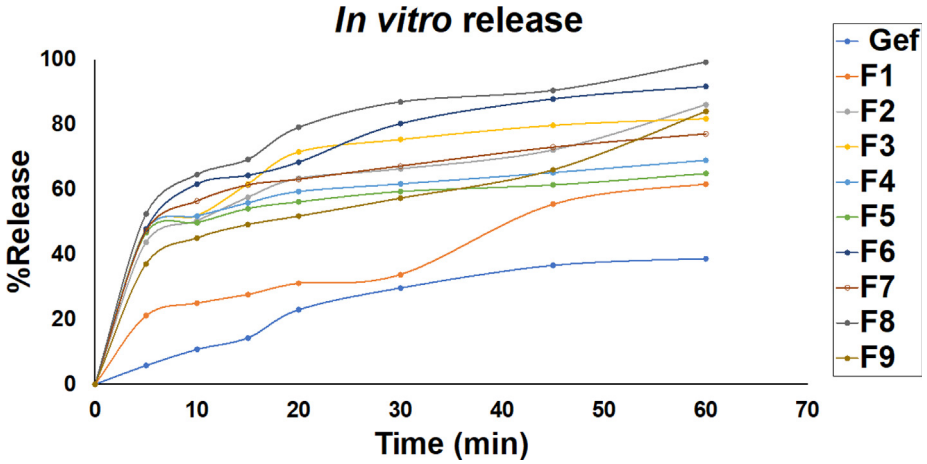

Fig. 13. *In vitro* drug release of the pure Gef and the 9 nanoformulations in FBS (pH of 5 at 37 °C and stirring rate of 100 rpm) using type II USP apparatus. Data are the mean of 3 determinations.

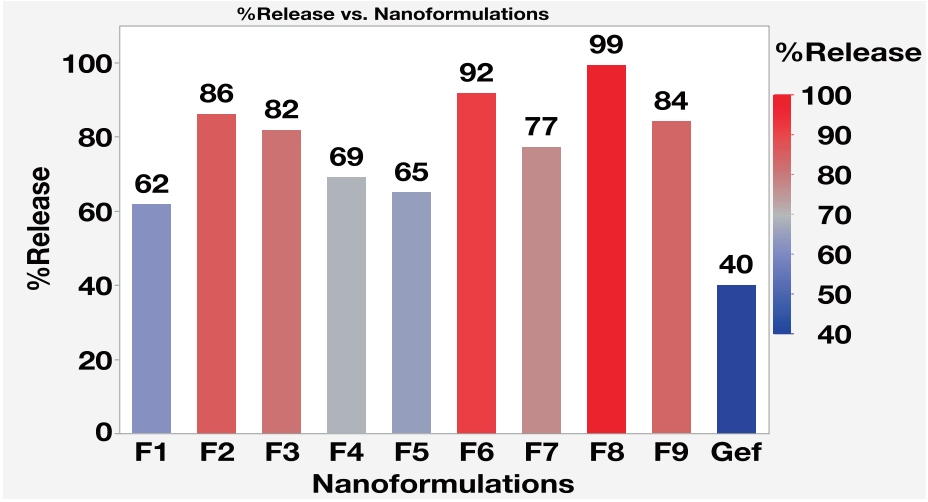

Fig.14. The %release of the pure Gef and the 9 nanoformulations. The data expressed as the mean %Release. (The optimized nanoformula is discriminated by red color).

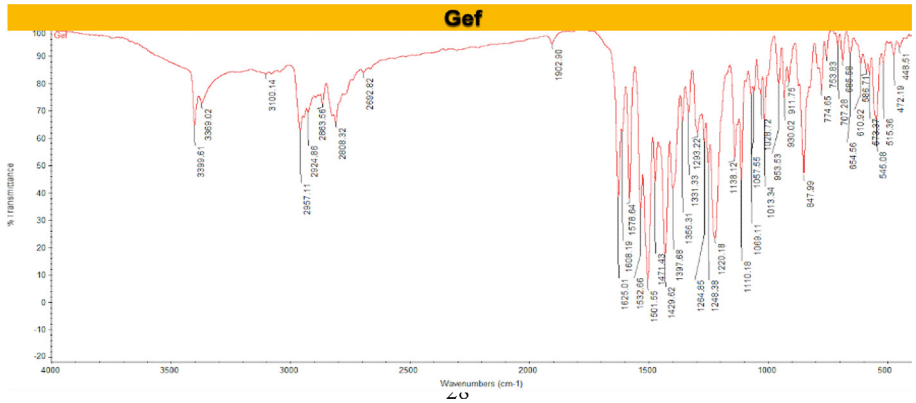

Fig.15a. FTIR spectrum of Gef.

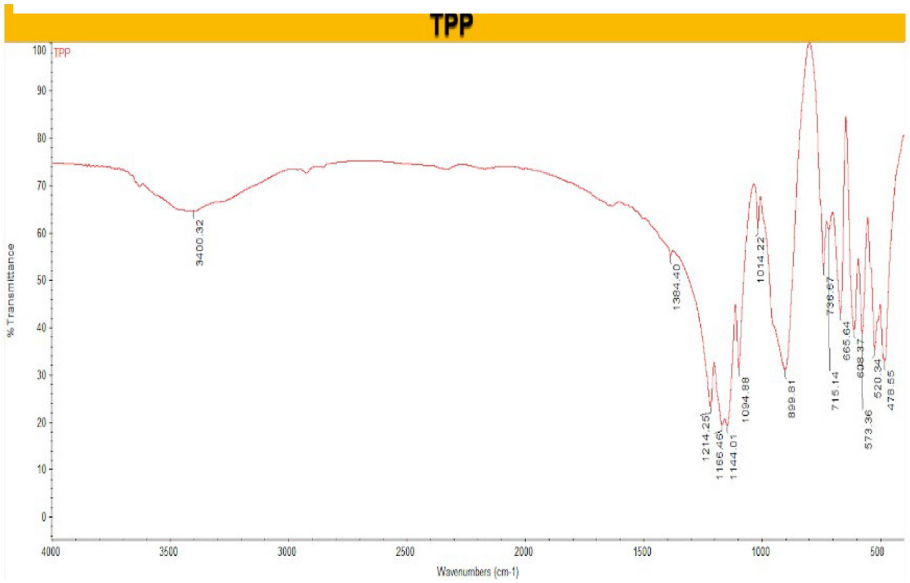

Fig. 15b. FTIR spectrum of TPP.

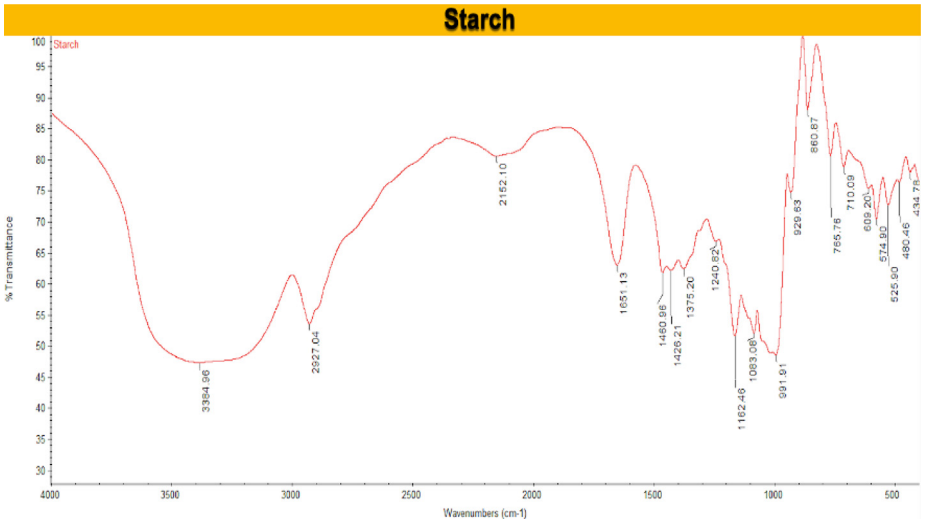

Fig. 15c. FTIR spectrum of soluble starch.

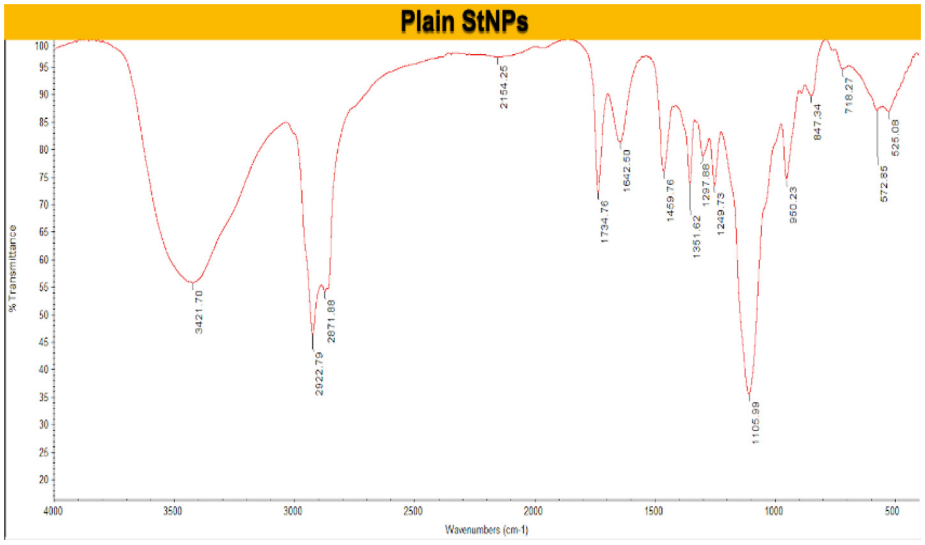

Fig. 15d. FTIR spectrum of plain StNPs.

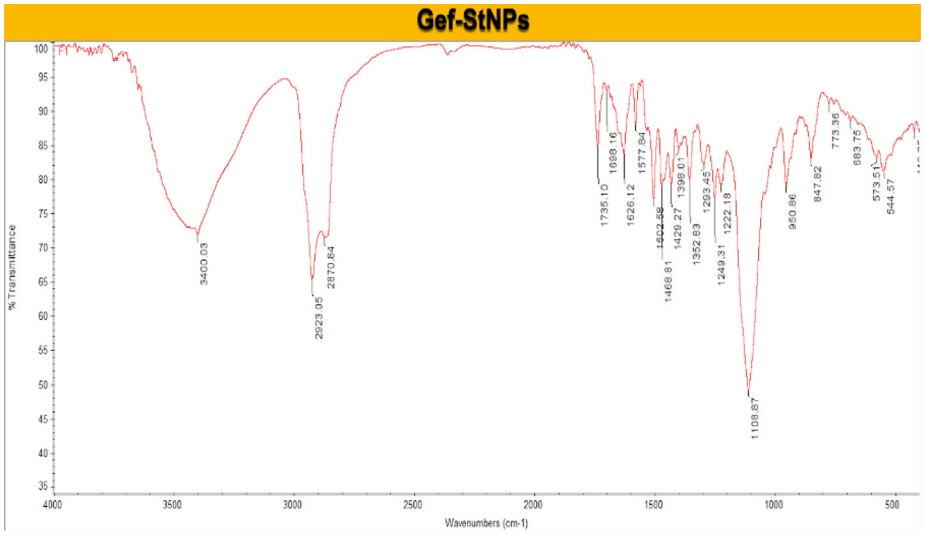

Fig. 15e. FTIR spectrum of Gef-StNPs.

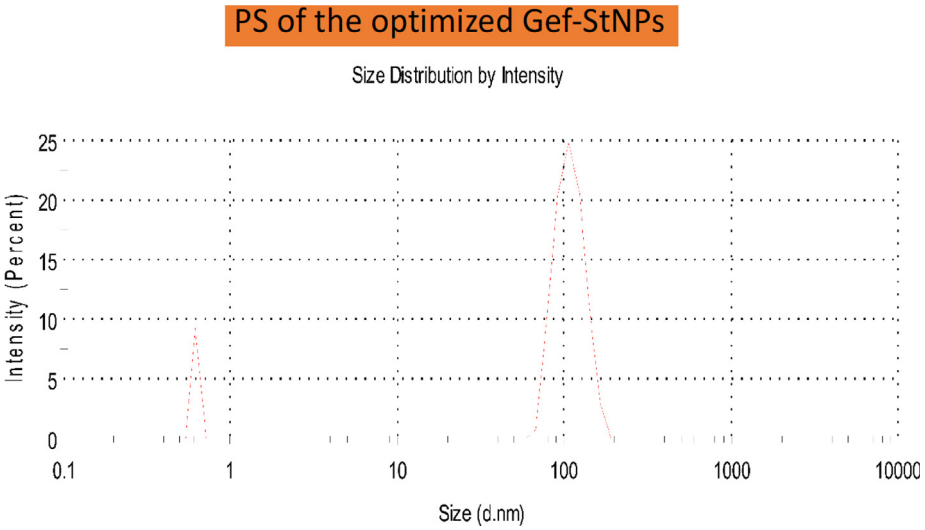

Fig. 16. The particle size distribution of the optimized Gef-StNPS by Dynamic Light Scattering.

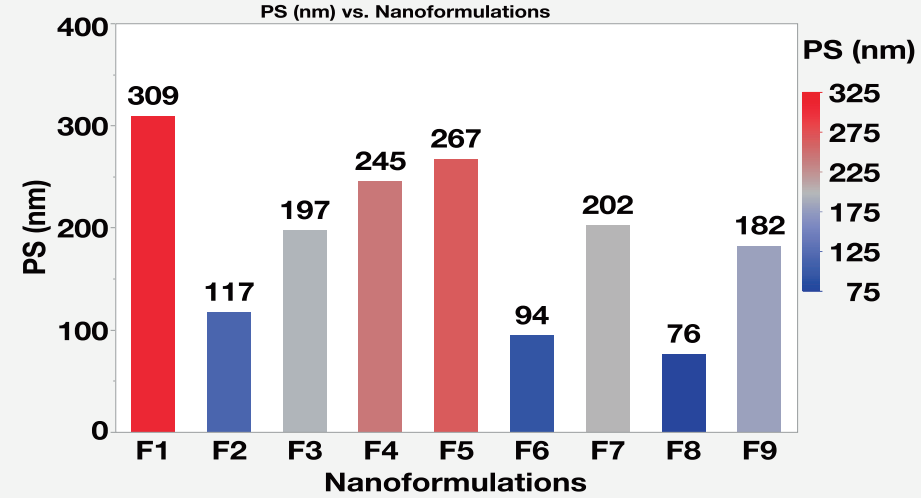

Fig. 17. PS of the 9 nanoformulations. The data expressed as the mean PS (The optimized nanoformula is discriminated by red color).

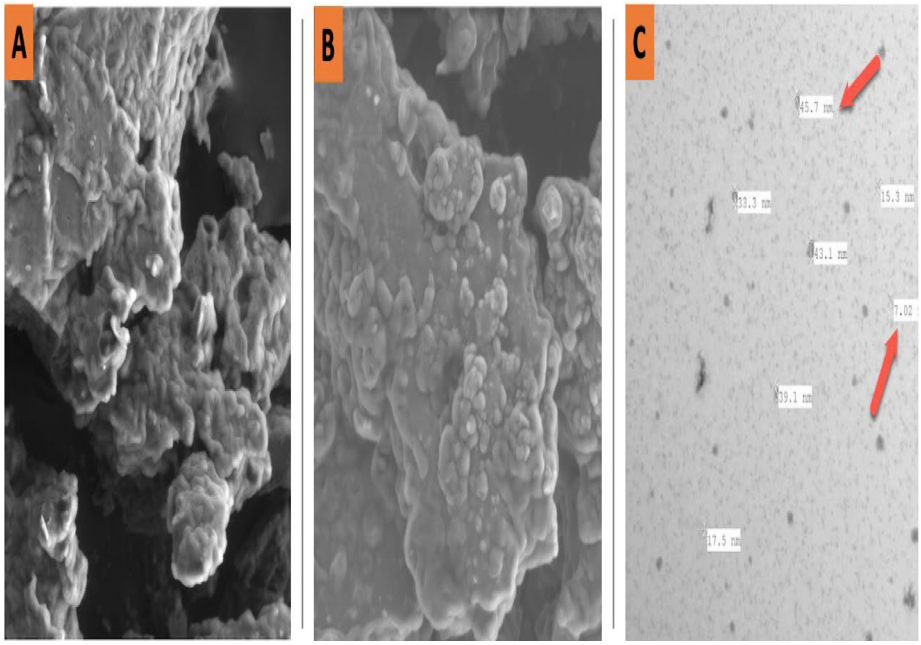

Fig. 18. SEM micrograph of plain StNPs (A), SEM micrograph of Gef-StNPs (B), and TEM micrograph of the optimized Gef-StNPs (C).

peaks were reported in previous studies (Alshetaili, 2021, W. Chen et al., 2018), which attributed to Gef crystallinity. Soluble starch diffraction patterns were observed with peaks at an angle from 10.277^0 to 54.310^0. Gef-StNPs diffraction patterns observed at angle range from 15.808^0 to 31.992^0. However, Gef-StNPs exhibited 2 sharp peaks at 24.279^0 (relative intensity = 90.9 %), and 26.371^0 (relative intensity = 100 %).

The sharp crystalline peaks of Gef disappeared from the diffractogram of Gef-StNPs indicating Gef encapsulation into the core of StNPs, while the fundamental peaks of starch are maintained, and the peaks intensity is minimized. Particularly notable is the diminishing of the peaks of Gef-StNPs which is ascribed to the existence of Gef in the amorphous phase.

3.7. In vitro cytotoxicity assay

3.7.1. Cell viability assay

The effect of Gef and Gef-StNPs on A549 cells viability was studied using the MTT assay. All experiments proceeded in triplicate. The IC_{50} value was calculated on the non-linear regression fit method by the GraphPad Prism software version 9.3.1. Cell viability was calculated using the following formula: (OD of Sample-OD of Blank)/ (OD of Control-OD of Blank) X100 (Eq.2).

OD is the optical density.

As shown in Figs. 21 and 22, Gef showed high cytotoxicity against A549 cells (IC_{50} = 21.65 ± 0.32 µg/mL), (Abdulkhaleq and Hassan Mohammed, n.d.) the cytotoxic effect was more

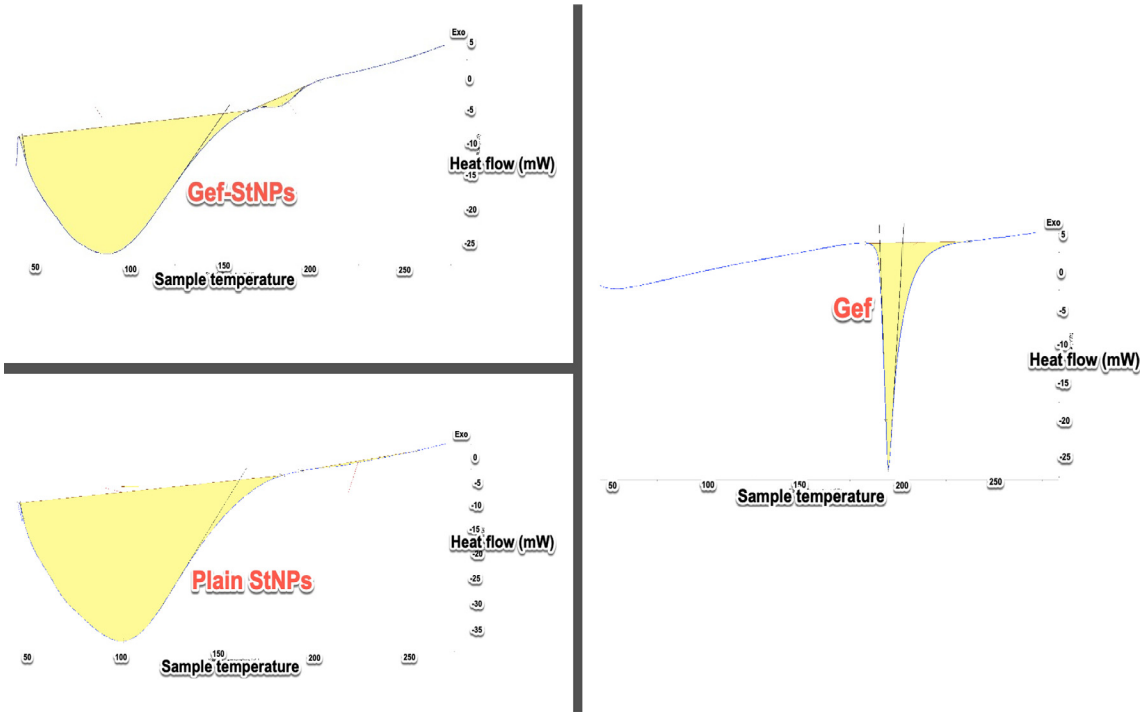

Fig. 19. DSC of the optimezd Gef-StNPs, plain StNPs and the pure Gef displaying the fading of the sharp endothermic peak of Gef due to the its effective encapsulation inside the StNPs.

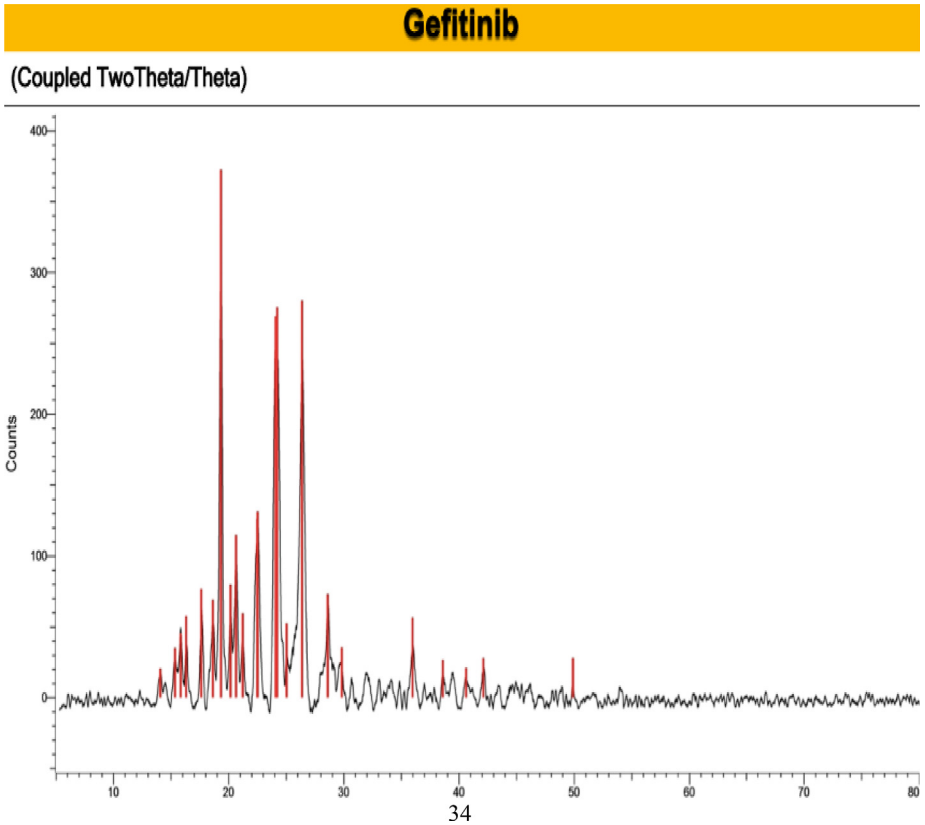

Fig. 20a. XRD of Gef with characteristic sharp diffraction peaks, reflecting Gef crystallinity.

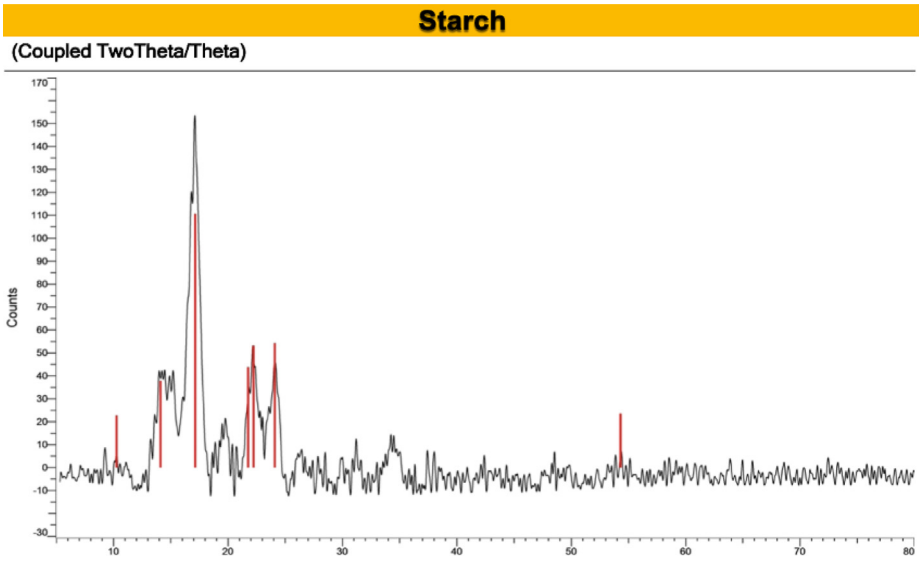

Fig. 20b. XRD of soluble starch.

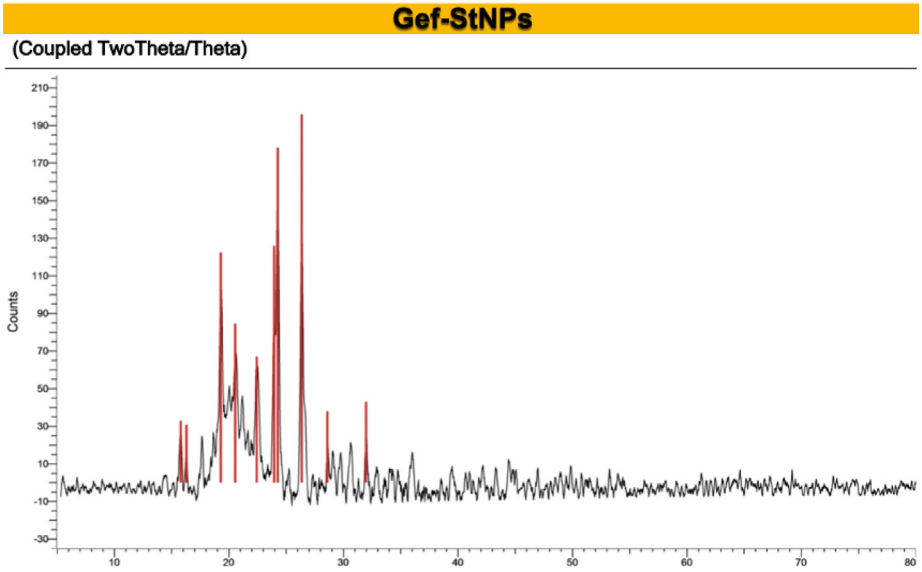

Fig. 20c. XRD of the optimized Gef-StNPs revealing the disappearance of the sharp crystalline peaks of Gef.

pronounced with Gef-StNPs with an IC_{50} value of > 3-fold lower compared to that of pure Gef (IC_{50} = 6.037 ± 0.24 µg/mL). Therefore, it's evident that Gef-StNPs had a more powerful inhibition of A549 cell growth than pure Gef. These results revealed that more Gef-StNPs could be internalized into A549 cells, leading to higher cytotoxicity by the accumulation of the drug in the cells. These data clarify that starch played a critical role as a nanocarrier for the delivery of Gef inside the tumor.

3.7.2. Apoptosis assay

Flow cytometry studies the mechanism of cell death. The flow cytometry scatter plot (Figs. 23a-23c and 24.) is composed of 4 quadrants, the first quadrant (Q3) represents the viable cells which neither attached to Annexin-V nor PI (Annexin-V negative and PI negative or double negative). The second quadrant (Q4) expresses the early apoptotic cells which can bind only to Annexin-V but not PI (Annexin-V positive and PI negative). The third quadrant (Q2) implies the late apoptotic cells, cells that are Annexin-V positive and PI-positive (double-positive). Besides apoptosis, some cells

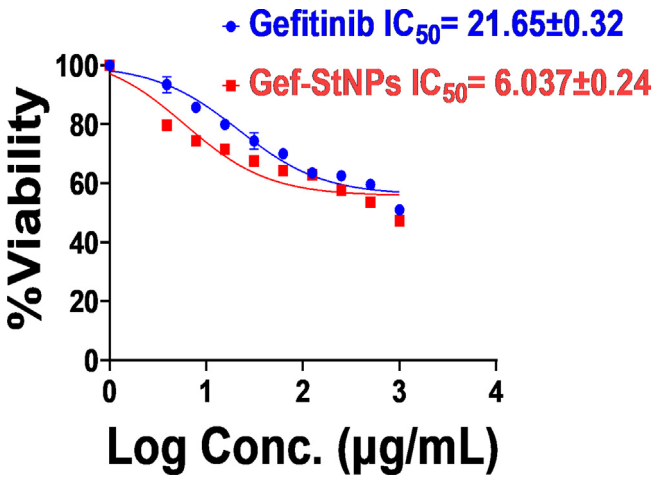

Fig. 21. Cell growth inhibition of free Gef and Gef-StNPs showing the powerful antiproliferative effect of the optimized Gef-StNPs compared to the pure Gef with IC_{50} of 6.037 ± 0.24 and 21.65 ± 0.32, respectively.

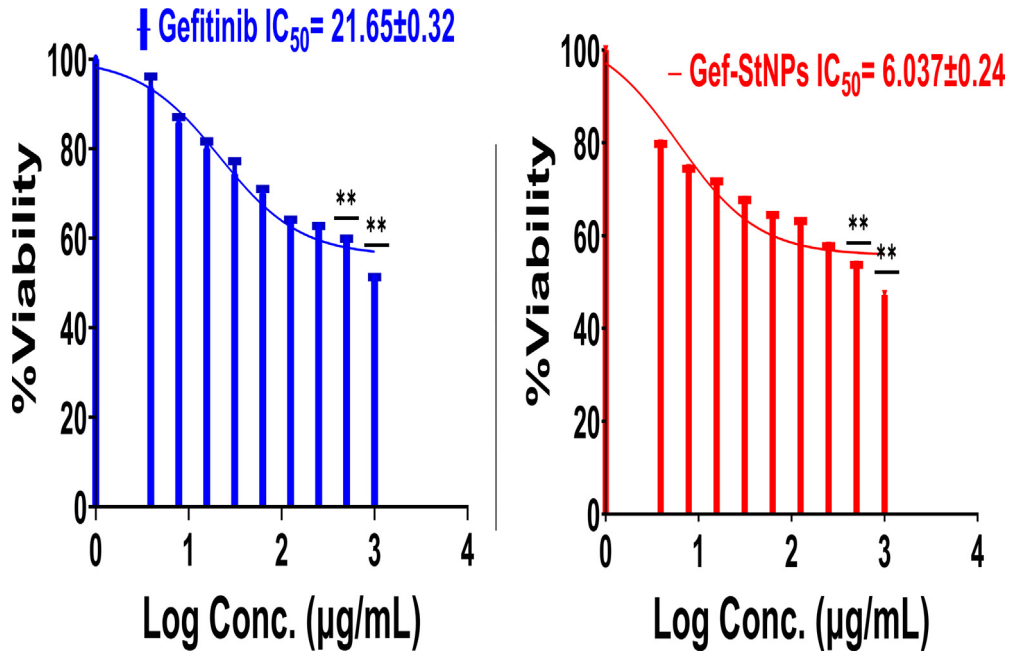

Fig. 22. Bar graph showing the %viability of Gef and Gef-StNPs showing the enhanced antiproliferative effect of the optimized Gef-StNPs compared to the pure Gef with IC_{50} = 6.037 ± 0.24 and 21.65 ± 0.32 respectively.

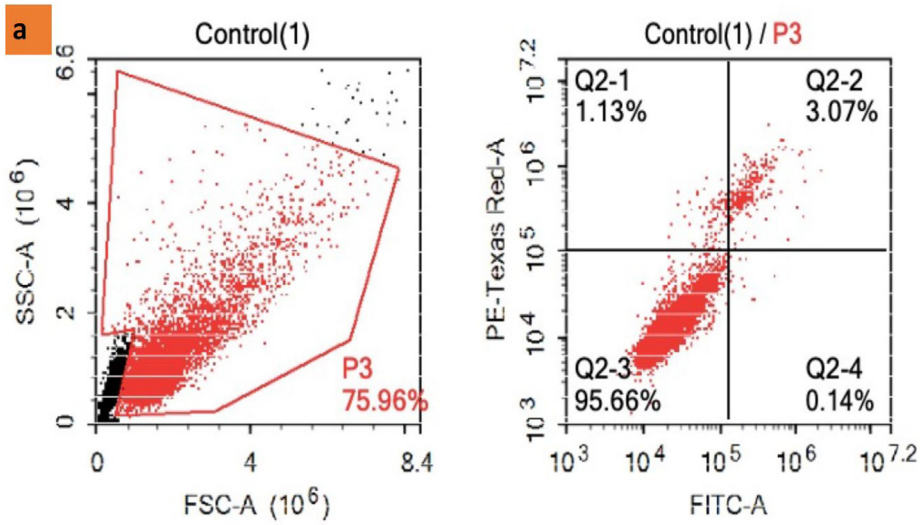

Fig. 23a. The scatter plot showing apoptosis of A549 cell populations exposed to doxorubicin (control), revealing %apoptosis of 3.07 ± 0.65 %. [necrotic cells(Q1), late apoptotic cells(Q2), healthy viable cells (Q3), and early apoptotic cells(Q4)].

may undergo necrosis (Q1), cells are Annexin-V negative and PI-positive. Applying this smart technique to study the mechanism of A549 cell death induced by Gef (Biswas et al., 2021)and Gef-StNPs. The assay confirmed the apoptosis in A549 cells exposed to Gef and Gef-StNPs.

Figs. 23 and 24 show that A549 cells, when exposed to doxorubicin (positive control), didn't show any significant apoptosis (3.0 7 ± 0.65 %); however, Gef and Gef-StNPs exposed A549 cells prompted higher apoptotic cell populations (29.38 ± 1.11 %) and (77.14 ± 1.43 %), respectively. These results confirm the MTT assay findings of the enhanced cytotoxicity produced by Gef-StNPs.

3.7.3. Cellular drug uptake

It is well-known that cancer cells have limited uptake of chemotherapeutics which is a reason for multidrug resistance (MDR). This MDR causes over 90 % of deaths in cancer patients

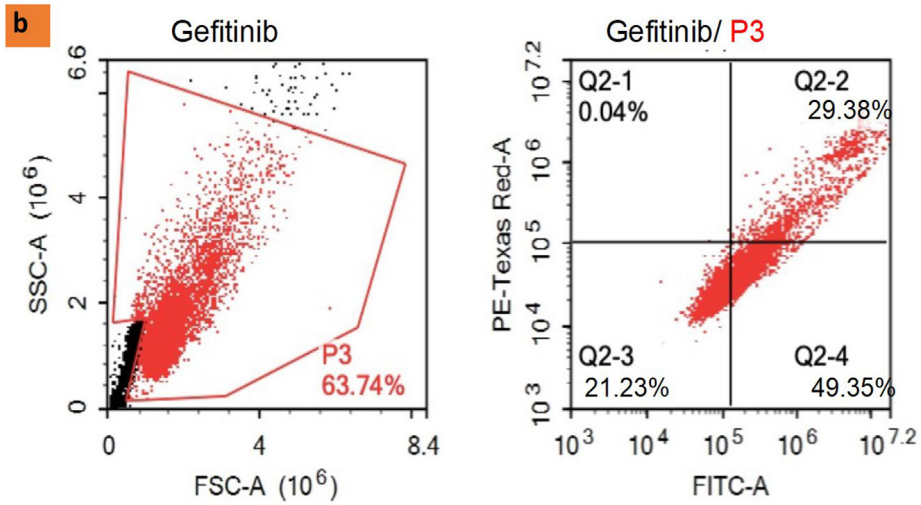

Fig. 23b. The scatter plot showing apoptosis of A549 cell populations exposed to the pure Gef, revealing %apoptosis of 29.38 ± 1.11 %. [necrotic cells(Q1), late apoptotic cells (Q2), healthy viable cells (Q3), and early apoptotic cells(Q4)].

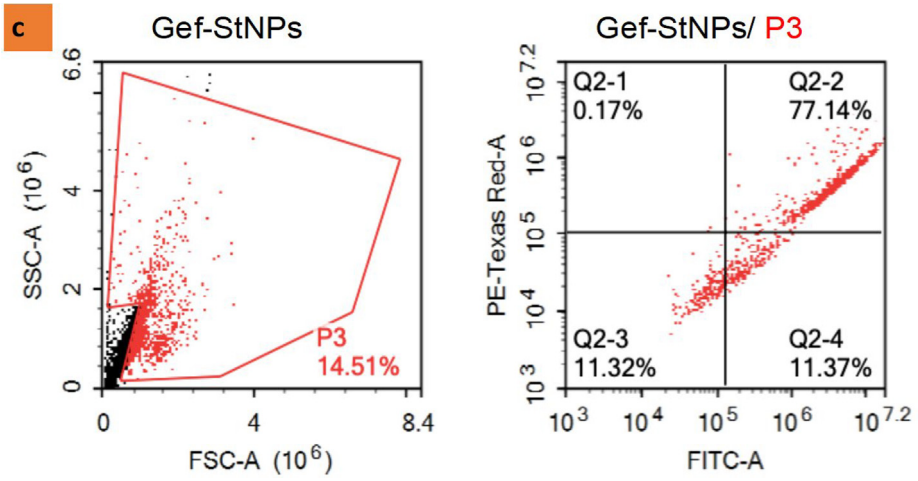

Fig. 23c. The scatter plot showing apoptosis of A549 cell populations exposed to the optimized Gef-StNPs, revealing %apoptosis of 77.14 ± 1.43 %. [necrotic cells(Q1), late apoptotic cells(Q2), healthy viable cells (Q3), and early apoptotic cells(Q4)].

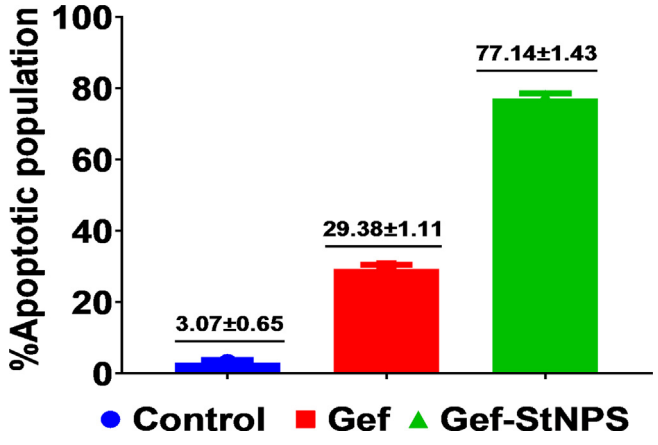

Fig. 24. The %apoptotic population elicited by Gef and Gef-StNPs was 29.38 ± 1.11 and 77.14 ± 1.43, respectively.

receiving traditional chemotherapeutics, therefore it is critical to engineer a system that could evade this MDR induced by cancer cells. It appeared that nanoparticles have this capability.

This was confirmed by comparing the uptake of pure Gef and Gef-StNPs inside A549 cells, utilizing HPLC (Markowicz-Piasecka et al., 2019; Tan et al., 2020), Fig. 25. First, a six-point calibration curve for Gef was conducted over a conc. range of 0.1–1 μg/mL (0.1, 0.2, 0.4, 06, 0.8, 1 μg/mL). The calculations were based on a plot of peak area vs concentration, Fig. 26. The results displayed in Fig. 27, demonstrate an uptake from Gef-StNPs more than double (3.976 ± 0.14 μg/mL) that achieved from pure Gef (1.777 ± 0. 1 μg/mL). These results emphasize the role of nanoparticles in combating lung cancer because of their higher degree of internalization inside tumor cells because smaller PS is easily uptaken by cancer cells.

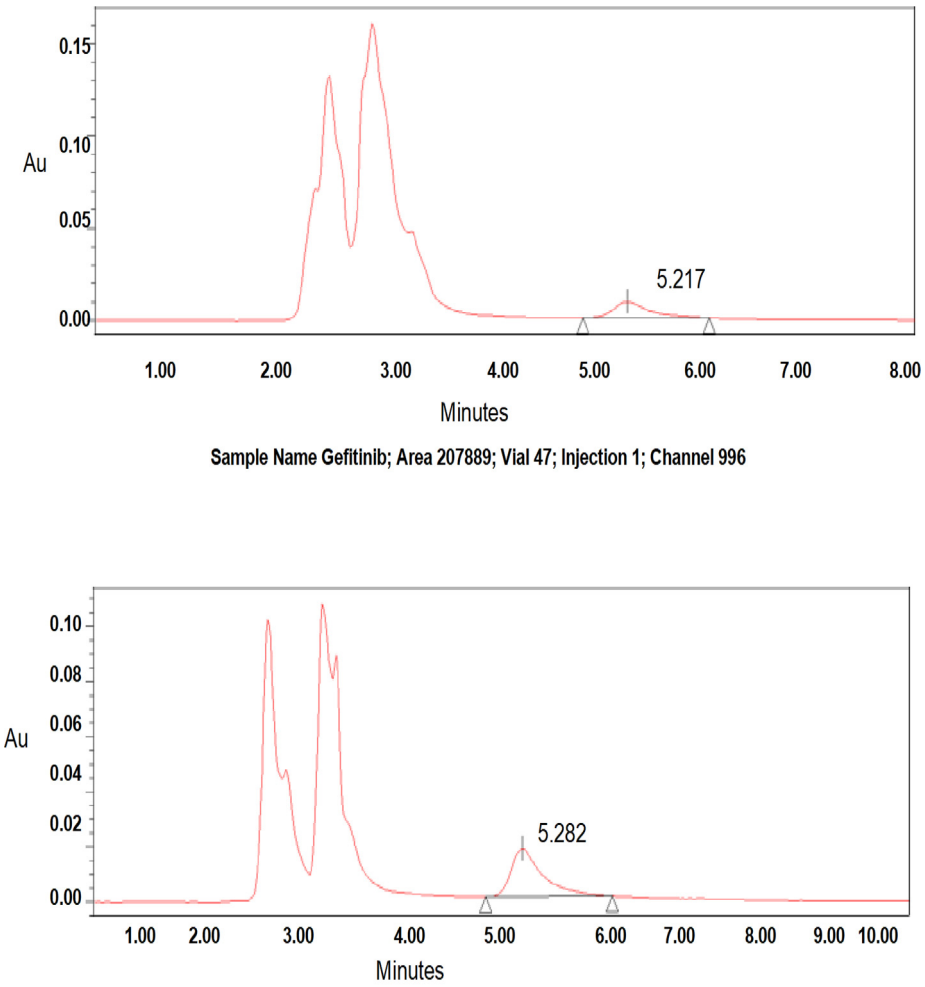

Fig. 25. HPLC chromatogram of Gef and the optimized Gef-StNPs.

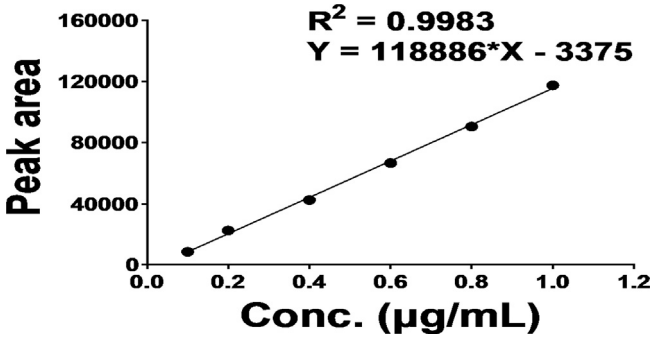

Fig. 26. HPLC calibration curve of the pure Gef.

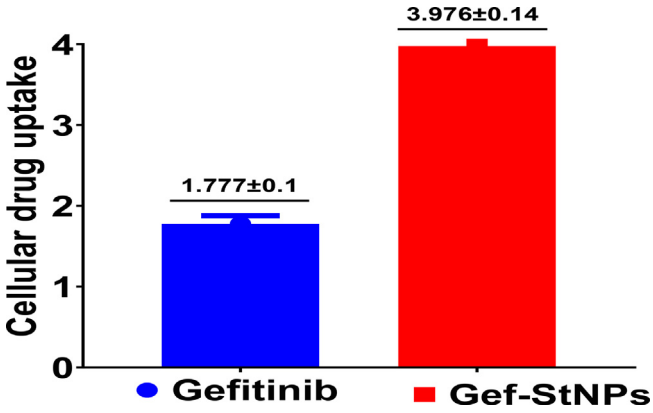

Fig. 27. The cellular uptake of Gef and Gef-StNPs into A549 human lung cancer cells displaying much higher uptake of Gef-StNPs due to its nano-size.

4. Conclusion

Every-five seconds, someone dies of cancer globally. The National Cancer Institute reported 135,720 deaths from lung cancer in the U.S. in 2020. These data have been flashing warning signs for governments, healthcare systems, and researchers. Researchers are thus racing to design an effective and safe therapy for lung cancer to erase the suffering of cancer patients. The failure of traditional chemotherapeutics has shifted researchers' focus towards nanoparticles. We used soluble starch nanoparticles to deliver Gef to cancer cells, preventing it from being in the wrong location. In return, this offers a reduction in side effects, improvement in solubility and bioavailability, better therapeutic control, higher cellular uptake into A549 cells, and greater cytotoxicity represented in a much higher apoptotic effect and cell growth inhibition. These outcomes demonstrate that the efficacy of Gef-StNPs is established beyond any reasonable doubt and a lot of hopes are hanging on nanoparticles derived from nature. Wrestling the cancer dragon to the ground looks to be a difficult task, but soluble starch nanoparticles create an opportunity.

Declaration of Competing Interest

The authors declare that they have no known competing financial interests or personal relationships that could have appeared to influence the work reported in this paper.

References

Abdulkhaleq, Z.M., Hassan Mohammed, M., n.d.. Molecular docking, synthesis, characterization and preliminary cytotoxic evaluation of new 1, 3,4-Thiadiazole derivatives as EGFR inhibitors. Mater. Today:. Proc. 65, 2490–2501.

Aghda, N., Ab, M., Tunnell, J.W., Ad, T., n.d. Design of smart nanomedicines for effective cancer treatment Graphical abstract.

Alshetaili, A.S., 2021. Gefitinib loaded PLGA and chitosan coated PLGA nanoparticles with magnified cytotoxicity against A549 lung cancer cell lines. Saudi J. Biol. Sci. 28, 5065–5073. https://doi.org/10.1016/j.sjbs.2021.05.025.

Anand, U., Dey, A., Chandel, A.K.S., Sanyal, R., Mishra, A., Pandey, D.K., de Falco, V., Upadhyay, A., Kandimalla, R., Chaudhary, A., Dhanjal, J.K., Dewanjee, S., Vallamkondu, J., Pérez de la Lastra, J.M., 2022. Cancer chemotherapy and beyond: current status, drug candidates, associated risks and progress in targeted therapeutics. Genes Dis. https://doi.org/10.1016/j.gendis.2022.02.007.

Arenas, L.T., Lima, E.C., dos Santos, A.A., Vaghetti, J.C.P., Costa, T.M.H., Benvenutti, E. v., 2007. Use of statistical design of experiments to evaluate the sorption capacity of 1,4-diazoniabicycle[2.2.2]octane/silica chloride for Cr(VI) adsorption. Colloids Surf. A Physicochem. Eng. Asp. 297, 240–248. https://doi.org/10.1016/j.colsurfa.2006.10.050.

Bade, B.C., Dela Cruz, C.S., 2020. Lung cancer 2020: epidemiology, etiology, and prevention. Clin. Chest Med. 41 (1), 1–24. https://doi.org/10.1016/j.ccm.2019.10.001.

Biswas, R., Yang, C.-M., Lu, W., He, J.i., Chen, T., Tian, F., Li, Y., 2021. Aidi injection, a traditional Chinese medicine extract, reverses Gefitinib resistance in non-small cell lung cancer cells. Eur. J. Integr. Med. 46, 101368.

Carmona-Garcia, R., Sanchez-Rivera, M.M., Méndez-Montealvo, G., Garza-Montoya, B., Bello-Pérez, L.A., 2009. Effect of the cross-linked reagent type on some morphological, physicochemical and functional characteristics of banana starch (Musa paradisiaca). Carbohydr. Polym. 76, 117–122. https://doi.org/10.1016/j.carbpol.2008.09.029.

Chen, W., di Carlo, C., Devery, D., McGrath, D.J., McHugh, P.E., Kleinsteinberg, K., Jockenhoevel, S., Hennink, W.E., Kok, R.J., 2018. Fabrication and characterization of gefitinib-releasing polyurethane foam as a coating for drug-eluting stent in the treatment of bronchotracheal cancer. Int. J. Pharm. 548, 803–811. https://doi.org/10.1016/j.ijpharm.2017.10.026.

Chen, K., Zhang, S., Wang, H., Wang, X., Zhang, Y., Yu, L., Ke, L., Gong, R., 2018. Fabrication of Doxorubicin-Loaded Glycyrrhetinic Acid-Biotin-Starch Nanoparticles and Drug Delivery Into HepG2 Cells In Vitro. Starch - Stärke 71 (3-4), 1800031. https://doi.org/10.1002/star.201800031.

Chin, S.F., Pang, S.C., Tay, S.H., 2011. Size controlled synthesis of starch nanoparticles by a simple nanoprecipitation method. Carbohydr. Polym. 86, 1817–1819. https://doi.org/10.1016/j.carbpol.2011.07.012.

Chin, S.F., Mohd Yazid, S.N.A., Pang, S.C., 2014. Preparation and characterization of starch nanoparticles for controlled release of curcumin. Int. J. Polym. Sci. 2014, 1–8. https://doi.org/10.1155/2014/340121.

da Silva Miranda Sechi, N., Marques, P.T., 2017. Preparation and physicochemical, structural and morphological characterization of phosphorylated starch, in: Materials Research. Universidade Federal de Sao Carlos, pp. 174–180. https://doi.org/10.1590/1980-5373-MR-2016-1008.

Dong, X., Liu, L.i., Wang, Y., Li, T., Wu, Z., Yuan, H., Ma, P., Shi, D., Chen, M., Dong, W., 2020. The compatibilization of poly (propylene carbonate)/poly (lactic acid) blends in presence of core-shell starch nanoparticles. Carbohydr. Polym. 254, 117321. https://doi.org/10.1016/j.carbpol.2020.117321.

El-Naggar, M.E., El-Rafie, M.H., El-sheikh, M.A., El-Feky, G.S., Hebeish, A., 2015. Synthesis, characterization, release kinetics and toxicity profile of drug-loaded starch nanoparticles. Int J Biol Macromol 81, 718–729. https://doi.org/10.1016/j.ijbiomac.2015.09.005.

El-Sheikh, M.A., 2017. New technique in starch nanoparticles synthesis. Carbohydr. Polym. 176, 214–219. https://doi.org/10.1016/j.carbpol.2017.08.033.

Galimont-Collen, A.F.S., Vos, L.E., Lavrijsen, A.P.M., Ouwerkerk, J., Gelderblom, H., 2007. Classification and management of skin, hair, nail and mucosal side-effects of epidermal growth factor receptor (EGFR) inhibitors. Eur. J. Cancer 43, 845–851. https://doi.org/10.1016/j.ejca.2006.11.016.

Garizo, A.R., Castro, F., Martins, C., Almeida, A., Dias, T.P., Fernardes, F., Barrias, C.C., Bernardes, N., Fialho, A.M., Sarmento, B., 2021. p28-functionalized PLGA nanoparticles loaded with gefitinib reduce tumor burden and metastases formation on lung cancer. J. Control. Release 337, 329–342. https://doi.org/10.1016/j.jconrel.2021.07.035.

Gidwani, B., Vyas, A., Deep Kaur, C., 2018. Investigation of inclusion behaviour of gefitinib with epichlorohydrin-β-cyclodextrin polymer: preparation of binary complex, stoichiometric determination and characterization. J. Pharm. Biomed. Anal. 160, 31–37. https://doi.org/10.1016/j.jpba.2018.07.025.

Gottipati, R., Mishra, S., 2010. Process optimization of adsorption of Cr(VI) on activated carbons prepared from plant precursors by a two-level full factorial design. Chem. Eng. J. 160, 99–107. https://doi.org/10.1016/j.cej.2010.03.015.

Gutiérrez, G., Morán, D., Marefati, A., Purhagen, J., Rayner, M., Matos, M., 2020. Synthesis of controlled size starch nanoparticles (SNPs). Carbohydr. Polym. 250, 116938.

Iyer, A.K., Khaled, G., Fang, J., Maeda, H., 2006. Exploiting the enhanced permeability and retention effect for tumor targeting. Drug Discov. Today 11 (17-18), 812–818. https://doi.org/10.1016/j.drudis.2006.07.005.

Jeannot, V., Gauche, C., Mazzaferro, S., Couvet, M., Vanwonterghem, L., Henry, M., Didier, C., Vollaire, J., Josserand, V., Coll, J.L., Schatz, C., Lecommandoux, S., Hurbin, A., 2018. Anti-tumor efficacy of hyaluronan-based nanoparticles for the co-delivery of drugs in lung cancer. J. Control. Release 275, 117–128. https://doi.org/10.1016/j.jconrel.2018.02.024.

Kim, J.H., Kim, J., Park, E.Y., Kim, J.-Y., 2017. Starch nanoparticles resulting from combination of dry heating under mildly acidic conditions and homogenization. Carbohydr. Polym. 168, 70–78. https://doi.org/10.1016/j.carbpol.2017.03.061.

Lin, C.-H., Chen, C.-H., Lin, Z.-C., Fang, J.-Y., 2017. Recent advances in oral delivery of drugs and bioactive natural products using solid lipid nanoparticles as the carriers. J. Food Drug Anal. 25 (2), 219–234. https://doi.org/10.1016/j.jfda.2017.02.001.

Lin, Q., Liu, G., Zhao, Z., Wei, D., Pang, J., Jiang, Y., 2017. Design of gefitinib-loaded poly (L-lactic acid) microspheres via a supercritical anti-solvent process for dry powder inhalation. Int. J. Pharm. 532, 573–580. https://doi.org/10.1016/j.ijpharm.2017.09.051.

Liu, G., Lin, Q., Huang, Y., Guan, G., Jiang, Y., 2017. Tailoring the particle microstructures of gefitinib by supercritical CO2 anti-solvent process. J. CO2 Util. 20, 43–51. https://doi.org/10.1016/j.jcou.2017.04.015.

Lopez-Silva, M., Agama-Acevedo, E., Bello-Perez, L.A., Alvarez-Ramirez, J., 2021. Influence of gelatinization degree and octenyl succinic anhydride esterification on the water sorption characteristics of corn starch. Carbohydr. Polym. 270,. https://doi.org/10.1016/j.carbpol.2021.118378 118378.

Manoi, K., Rizvi, S.S.H., 2010. Physicochemical characteristics of phosphorylated cross-linked starch produced by reactive supercritical fluid extrusion. Carbohydr. Polym. 81, 687–694. https://doi.org/10.1016/j.carbpol.2010.03.042.

Markowicz-Piasecka, M., Huttunen, J., Sikora, J., Huttunen, K.M., 2019. Sulfenamide derivatives can improve transporter-mediated cellular uptake of metformin and induce cytotoxicity in human breast adenocarcinoma cell lines. Bioorg. Chem. 87, 321–334. https://doi.org/10.1016/j.bioorg.2019.03.036.

Martins, J.P., das Neves, J., de la Fuente, M., Celia, C., Florindo, H., Günday-Türeli, N., Popat, A., Santos, J.L., Sousa, F., Schmid, R., Wolfram, J., Sarmento, B., Santos, H.A., 2020. The solid progress of nanomedicine. Drug Deliv. Transl. Res. 10 (3), 726–729. https://doi.org/10.1007/s13346-020-00743-2.

Nayek, S., Raghavendra, N.M., Sajeev Kumar, B., 2021a. Development of novel S PC-3 gefitinib lipid nanoparticles for effective drug delivery in breast cancer. tissue distribution studies and cell cytotoxicity analysis. J. Drug Deliv. Sci. Technol. 61, 102073.

Nayek, S., Scholar, R., Raghavendra, N.M., Sajeev Kumar, B., 2021b. Development of novel S PC-3 gefitinib lipid nanoparticles for effective drug delivery in breast cancer. tissue distribution studies and cell cytotoxicity analysis. J. Drug Deliv. Sci. Technol. 61, 1773–2247. https://doi.org/10.1016/j.jddst.2020.102073.

Peterson, L.L., Hurria, A., Feng, T., Mohile, S.G., Owusu, C., Klepin, H.D., Gross, C.P., Lichtman, S.M., Gajra, A., Glezerman, I., Katheria, V., Zavala, L., Smith, D.D., Sun, C.L., Tew, W.P., 2017. Association between renal function and chemotherapy-related toxicity in older adults with cancer. J. Geriatr. Oncol. 8, 96–101. https://doi.org/10.1016/J.JGO.2016.10.004.

Phillip Lee, Y.H., Sathigari, S., Jean Lin, Y.J., Ravis, W.R., Chadha, G., Parsons, D.L., Rangari, V.K., Wright, N., Babu, R.J., 2009. Gefitinibcyclodextrin inclusion complexes: physico-chemical characterization and dissolution studies Gefitinibcyclodextrin inclusion complexes. Drug Dev. Ind. Pharm. 35, 1113–1120. https://doi.org/10.1080/03639040902783074.

Sadeghi, R., Daniella, Z., Uzun, S., Kokini, J., 2017. Effects of starch composition and type of non-solvent on the formation of starch nanoparticles and improvement of curcumin stability in aqueous media. J. Cereal Sci. 76, 122–130. https://doi.org/10.1016/j.jcs.2017.05.020.

Scolari, I.R., Páez, P.L., Sánchez-Borzone, M.E., Granero, G.E., 2019. Promising Chitosan-Coated Alginate-Tween 80 Nanoparticles as Rifampicin Coadministered Ascorbic Acid Delivery Carrier Against Mycobacterium tuberculosis. AAPS PharmSciTech. 20. https://doi.org/10.1208/s12249-018-1278-7.

Seyed Shahabadi, S.M., Reyhani, A., 2014. Optimization of operating conditions in ultrafiltration process for produced water treatment via the full factorial design methodology. Sep. Purif. Technol. 132, 50–61. https://doi.org/10.1016/j.seppur.2014.04.051.

Shokri, A., 2018. Application of Sono–photo-Fenton process for degradation of phenol derivatives in petrochemical wastewater using full factorial design of experiment. Int. J. Industrial Chem. 9, 295–303. https://doi.org/10.1007/s40090-018-0159-y.

Shokri, A., 2019. Employing Sono-Fenton Process for Degradation of 2-Nitrophenol in Aqueous Environment Using Box-Behnken Design Method and Kinetic Study. Russ. J. Phys. Chem. A 93, 243–249. https://doi.org/10.1134/S003602441902002X.

Shokri, A., 2020. Degradation of 4-Chloro phenol in aqueous media thru UV/Persulfate method by Artificial Neural Network and full factorial design method. Int. J. Environ. Anal. Chem. 1–15. https://doi.org/10.1080/03067319.2020.1791328.

Suchomel, P., Kvitek, L., Prucek, R., Panacek, A., Halder, A., Vajda, S., Zboril, R., 2018. Simple size-controlled synthesis of Au nanoparticles and their size-dependent catalytic activity. Sci. Rep. 8. https://doi.org/10.1038/s41598-018-22976-5.

Sukumar, U.K., Bhushan, B., Dubey, P., Matai, I., Sachdev, A., Packirisamy, G., 2013. Emerging applications of nanoparticles for lung cancer diagnosis and therapy. Int. Nano Lett. 3. https://doi.org/10.1186/2228-5326-3-45.

Tan, S.W., Israf Ali, D.A.B., Khaza'ai, H., Wong, J.W., Vidyadaran, S., 2020. Cellular uptake and anti-inflammatory effects of palm oil-derived delta (δ)-tocotrienol in microglia. Cell Immunol. 357, 104200. https://doi.org/10.1016/j.cellimm.2020.104200.

Thi, T., Duyen, M., van Hung, P., 2021. Morphology, crystalline structure and digestibility of debranched starch nanoparticles varying in average degree of polymerization and fabrication methods. Carbohydr. Polym. 256. https://doi.org/10.1016/j.carbpol.2020.117424.

Wang, X., Huang, L., Zhang, C., Deng, Y., Xie, P., Liu, L., Cheng, J., 2020. Research advances in chemical modifications of starch for hydrophobicity and its applications: a review. Carbohydr. Polym. 240, 116292. https://doi.org/10.1016/j.carbpol.2020.116292.

Wang, K., Purushotham, S., Lee, J.Y., Na, M.H., Park, H., Oh, S.J., Park, R.W., Park, J.Y., Lee, E., Cho, B.C., Song, M.N., Baek, M.C., Kwak, W., Yoo, J., Hoffman, A.S., Oh, Y.K., Kim, I.S., Lee, B.H., 2010. In vivo imaging of tumor apoptosis using histone H1-targeting peptide. J. Control. Release 148, 283–291. https://doi.org/10.1016/j.jconrel.2010.09.010.

Wolfram, J., Ferrari, M., 2019. Clinical cancer nanomedicine. Nano Today 25, 85–98. https://doi.org/10.1016/j.nantod.2019.02.005.

Xia, W., He, D.-N., Fu, Y.-F., Wei, X.-y., Liu, H.-C., Ye, J.-P., Liu, Y.-F., Li, J.-H., 2017. Advanced technology for nanostarches preparation by high speed jet and its mechanism analysis. Carbohydr. Polym. 176, 127–134. https://doi.org/10.1016/j.carbpol.2017.08.072.

Xia, W., Zheng, B., Li, T., Lian, F., Lin, Y., Liu, R., 2020. Fabrication, characterization and evaluation of myricetin adsorption onto starch nanoparticles. Carbohydr. Polym. 250, 116848.